Title: Interferon-independent STING enforces epithelial genome-integrity checkpoint to restrain tumor evolution

Authors: Hang Xiang[1,2†], Martina Macino[3,10,12†], Clemens Woitaske-Proske[4], Nicholas Bodenstein[5], Joana P Bernardes[1], Florian Tran[1], Nicole A. Schmid[6], Gabriela Rios Martini[7], Felix Wottawa[1], Johanna Bornhaeuser[1], Nassim Kakavand[1], Oliver Dyck Dionisi[3], Silke van den Bossche[1], Guang Yang[1], Qicong Wu[1], Julia Kugler[1], Lina Welz[1,2], Bjorn Konukiewitz[8], Julius C. Fischer[6], Christian Peifer[4], Stefan Schreiber[1,2], Philip Rosenstiel[1], Markus Tschurtschenthaler[5,9], Ashley D Sanders[3,11,12*] and Konrad Aden[1,2*]

Funding:

This work was supported by the BMBF iTREAT project (P.R.), DFG Cluster of excellence "Precision medicine in chronic inflammation" TI-1 and TI-5 the EKFS research grant #2019_A09, EKFS Clinician Scientist Professorship (K.A.) and the EKFK Clinician Scientist School (HALT), the BMBF (eMED Juniorverbund "Try-IBD" 01ZX1915A), the DFG RU5042 (P.R., K.A.), the DFG "SFB 1371 - Microbiome signatures", #395357507 (M.T., J.C.F.) and German Cancer Aid (TargHet, #70115995 to M.T.).

Author Contributions:

Conceptualization: KA, HX

Methodology: KA, HX

Investigation: HX, MM, CW, NB, NAS, FW, JB, FT, NK, JB, SV, GY, QW, CP, JK, LW, BK, SS, PR, MT, KA

Supervision: PR, KA

Writing – original draft: HX, KA

Writing – review & editing: PR, SS, MT, AS, MM, NB

Competing interests: The authors have no conflict of interest.

Data, code, and materials availability: The data that support the findings of this study

are available from the corresponding author upon reasonable request. Sequencing data will be deposited in a public repository and made available upon publication. Accession numbers will be provided prior to publication.

Affiliations:

[1] Institute of Clinical Molecular Biology, Christian-Albrechts-University of Kiel and University Hospital Schleswig-Holstein; Kiel, Germany.

[2] Department of Internal Medicine I, University Medical Center Schleswig-Holstein; Kiel, Germany.

[3] Berlin Institute for Medical Systems Biology (BIMSB), Max Delbrück Center for Molecular Medicine in the Helmholtz Association (MDC); Berlin, Germany.

[4] Institute of Pharmaceutical Chemistry, Christian-Albrechts-University of Kiel; Kiel, Germany.

[5] Institute of Experimental Cancer Therapy, Center for Translational Cancer Research (TranslaTUM), TUM University Hospital, School of Medicine and Health, Technical University of Munich; Munich, Germany.

[6] Department of Radiation Oncology, TUM University Hospital, School of Medicine and Health, Technical University of Munich; Munich, Germany.

[7] Institute of Immunology, Christian-Albrechts-University of Kiel and University Hospital Schleswig-Holstein; Kiel, Germany.

[8] Department of Pathology, Christian-Albrechts-University of Kiel and University Hospital Schleswig-Holstein; Kiel, Germany.

[9] Division of Translational Cancer Research, German Cancer Research Center (DKFZ) and German Cancer Consortium (DKTK); Heidelberg, Germany.

[10] Humboldt-Universität zu Berlin, Institut für Biologie; Berlin, Germany.

[11] Charité – Universitätsmedizin Berlin, corporate member of Freie Universität Berlin and Humboldt-Universität zu Berlin; Berlin, Germany.

[12] Berlin Institute of Health (BIH) at Charité – Universitätsmedizin Berlin; Berlin, Germany.

*Corresponding author. Email: Ashley.Sanders@mdc-berlin.de; k.aden@ikmb.uni-kiel.de

† These authors contributed equally to this work

Abstract:
STING is canonically known for mediating interferon responses to cytosolic DNA, yet its cell-intrinsic role in genome maintenance beyond the immune context is unknown. Here we show that epithelial STING functions as a type I interferon-independent genome-integrity checkpoint. STING loss impairs homologous recombination repair, attenuates ATM-associated damage signaling, elevates CDK1 activity, and causes chromosomal instability revealed by single-cell Strand-seq, culminating in spontaneous intestinal adenocarcinoma. These defects arise before tumor formation and confer selective vulnerability to CDK inhibition in tumor organoids and human colorectal cancer cells. Our findings identify STING as a cell-autonomous guardian of epithelial genome stability that restrains chromosomal instability-driven tumor evolution beyond its canonical immune function.

Main Text:
The intestinal mucosa is a highly proliferative tissue that constantly renews the epithelial lining into specified cell types to meet the different physiological demands in a healthy state (*1*). However, during DNA replication, DNA polymerases frequently misincorporate ribonucleotides into the genome, and in the absence of efficient ribonucleotide excision repair (RER) these lesions can accumulate to >1,000,000 sites per genome, making them one of the most abundant naturally occurring replication errors (*2*). Failure of RER, which removes misincorporated ribonucleotides from genomic DNA via the enzyme RNase H2, leads to DNA damage and subsequent activation of p53 as a major tumor suppressor, resulting in loss of proliferation and induction of cellular senescence (*2, 3*). We and others have shown that several key cellular homeostatic factors (ER-stress, Autophagy) are able to modify the p53-dependent tumor suppression, resulting in genomic instability and transcription-associated mutagenesis (*4, 5*). Importantly, failure of RER not only leads to induction of DNA damage confined to the nucleus but also activates the cGAS-STING pathway through to the accumulation of cytosolic micronuclei containing damaged dsDNA (*6*). dsDNA sensing by cGAS-STING pathway results in the activation of a canonical innate immune response, involving phosphorylation of Tank-binding protein (TBK),

92 Interferon-related factor 3 (IRF) and subsequent induction of type I interferon (IFN-I)
93 (*7*). Beyond its canonical role in innate immune signaling, cGAS itself has been
94 described to modulate DNA repair pathways. In both mice and humans, cGAS can
95 inhibit homologous recombination (HR) by interfering with RAD51-mediated repair,
96 whereas a 4 amino acid change in the naked mole cGAS potentiates DNA repair via
97 enhanced homologous recombination, which may contribute to its cancer resistance (*8,*
98 *9*). Notably, the reported cGAS-STING effects on HR appear to be context-dependent
99 and remain controversial. Along the same line, cGAS-derived cGAMP has been
100 reported to trigger DNA damage signaling, supporting a broader role of the cGAS-
101 STING axis in genome maintenance (*10*). However, the exact mechanism by which
102 STING-dependent dsDNA sensing facilitates DNA repair is not understood. In addition,
103 the anti-tumor role of cGAS-STING is mostly viewed in the context of anti-tumor
104 immunity in immune cells, in which therapeutic stimulation of STING is investigated
105 as an adjunct therapy in cancers such as prostate cancer (*11-14*). In addition, whether
106 STING also acts in an epithelial-intrinsic manner to sense DNA damage induced by
107 RER failure and preserve genome integrity is not known. It has been previously
108 reported that functional STING signaling is abrogated in colorectal cancer, but whether
109 this is mechanistically linked to preservation of genome integrity is unknown (*15, 16*).
110 Here, we identify epithelial STING as a cell-intrinsic genome-stability factor that
111 supports ataxia-telangiectasia mutated (ATM) activation and HR competence, restrains
112 chromosomal instability, and suppresses intestinal tumorigenesis.

113 **Epithelial STING protects against spontaneous intestinal tumorigenesis**

114 It has been previously established that RNase H2b deficiency induces the accumulation
115 of cytosolic dsDNA, which potentially activate the cGAS-STING pathway (*17*). We
116 first assessed epithelial STING expression in the intestine of 8-12-week-old $H2b^{\Delta IEC}$
117 mice, in which *Rnaseh2b* is selectively deleted in intestinal epithelial cells, and
118 compared with $H2b^{fl/fl}$ control mice (*3, 4*). $H2b^{\Delta IEC}$ mice showed a significant increase
119 in Crypt-based intestinal epithelial cells expressing STING, compared to $H2b^{fl/fl}$
120 controls (**Fig. 1A, B**), along with elevated STING protein levels in small intestinal
121 organoids derived from $H2b^{\Delta IEC}$ mice (**Fig. 1C**). These findings suggest a direct
122 association between epithelial DNA damage and STING induction.

123 To investigate a potential link between DNA damage repair and cGAS-STING
124 signaling in intestinal epithelial cells (IECs), we generated CRISPR/Cas9-mediated
125 MODE-K knockout lines targeting either *Tmem173* (STING$^{-/-}$) or cGAS (cGAS$^{-/-}$) (**fig.**
126 **S1A-B**). DNA damage was induced by either *Rnaseh2b* knockdown or cytarabine
127 (AraC) treatment. Under both conditions, cGAS$^{-/-}$ and STING$^{-/-}$ cells showed markedly
128 reduced cGAS-STING signaling, including diminished TBK1 phosphorylation and
129 reduced induction of interferon inducible genes (**Fig. 1D, fig. S2A-G**). These findings
130 indicate that RER impairment activates cGAS-STING-dependent signaling in intestinal
131 epithelial cells.

132 To investigate the tumor-suppressive role of epithelial STING *in vivo* in the context of
133 RNase H2b deficiency-induced DNA damage, we generated *H2b*$^{\Delta IEC}$/*STING*$^{-/-}$ mice in
134 which Tmem173 is additionally ablated and monitored intestinal tumor development in
135 aged animals (>53 weeks) (**Fig. 1E, fig. S1C-D**). *H2b*$^{\Delta IEC}$/*STING*$^{-/-}$ mice exhibited a
136 markedly increased tumor incidence (16/37) compared with *H2b*$^{fl/fl}$ (0/12), *H2b*$^{\Delta IEC}$
137 (2/23), or *STING*$^{-/-}$ (2/18) controls, along with a significant increase of tumors per
138 mouse (**Fig. 1F-H**). Notably, all intestinal tumors in *H2b*$^{\Delta IEC}$/*STING*$^{-/-}$ mice were
139 adenocarcinomas localized to the small intestine, predominantly affecting the
140 duodenum (45.7%) and jejunum (45.7%) (**Fig. 1I-K**). In addition, *H2b*$^{\Delta IEC}$/*STING*$^{-/-}$
141 mice exhibited shortened colon and small intestine length, while body and liver weight
142 were unchanged compared to *H2b*$^{fl/fl}$ (**fig. S3A-D**).

143 To test whether STING loss within the intestinal epithelium is sufficient to drive
144 tumorigenesis under DNA damage, we generated mice with epithelial-specific deletion
145 of STING on the *H2b*$^{\Delta IEC}$ background (*H2b*/*STING*$^{\Delta IEC}$). At baseline, these mice closely
146 resembled systemic knockout animals (**fig. S3A-H**) and developed spontaneous small-
147 intestinal adenocarcinomas (3/7) with comparable incidence and histology (**Fig. 1G-J**),
148 indicating that tumorigenesis arises from epithelial STING loss.

149 As additional evidence of aggressiveness, tumor-derived organoids from
150 *H2b*$^{\Delta IEC}$/STING$^{-/-}$ mice formed malignant orthotopic tumors after transplantation into
151 the colonic mucosa of immunodeficient NSG mice, and organoids from one primary
152 tumor gave rise to liver metastases in recipient animals (**fig. S3I-L**). Collectively, these
153 findings identify STING as a protective factor in the intestinal epithelium that limits

154 chronic DNA damage-driven transformation and restrains spontaneous small-bowel
155 adenocarcinoma formation.

156 **Loss of STING results in chromosomal instability and clonal expansion in**
157 **intestinal epithelium**

158 The spontaneous tumor phenotype prompted us to investigate whether STING loss
159 destabilizes the epithelial genome at single-cell resolution. To directly assess this, we
160 performed Strand-seq, to quantify the rate and formation of genetic aberrations on a
161 cell-by-cell basis in small intestinal organoids derived from *H2b*$^{fl/fl}$, *H2b*$^{\Delta IEC}$ and
162 *H2b*$^{\Delta IEC}$/*STING*$^{-/-}$ mice (**fig. S4A**). Strand-seq is a single-cell DNA sequencing method
163 designed to detect structural rearrangements and sister chromatid exchanges (SCEs)
164 arising in mitotic cells (*18-21*). Because SCEs reflect crossover events generated during
165 HR repair of double-strand break (DSB), and manifest as strand-state changes or
166 breakpoints (BPs) in Strand-seq data (*21*), they provide a quantitative readout of HR-
167 associate genome instability (**fig. S4B-C, fig. S5**).

168 We found a significant increase in the total number of BPs per cell in *H2b*$^{\Delta IEC}$ cells
169 (median= 6, range= 1-113, p= 7.6e-07) as compared to *H2b*$^{fl/fl}$ control cells (median =
170 3, range= 0-10) indicating an elevated rate of SCE formation under *H2b* deficiency.
171 This phenotype was further exacerbated by additional STING loss with
172 *H2b*$^{\Delta IEC}$/*STING*$^{-/-}$ cells showing a median= 44 BPs per cell (range= 5-67, p= <2.22e-16)
173 (**Fig. 2A-B**). To clearly distinguish genomically unstable cells, we defined a threshold
174 of >10 BPs based on the upper distribution of *H2b*$^{fl/fl}$ cells. Using this cutoff, *H2b*$^{\Delta IEC}$
175 cells segregated into two subpopulations, with 34% classified as unstable (>10 BPs;
176 median = 41 BPs/cell; p= 3.72e-10 vs *H2b*$^{fl/fl}$), whereas 90% of *H2b*$^{\Delta IEC}$/*STING*$^{-/-}$ cells
177 exceeded this threshold (median = 45 BPs/cell) (**Fig. 2B-C**). Notably, among the
178 unstable cells, *H2b*$^{\Delta IEC}$ and *H2b*$^{\Delta IEC}$/*STING*$^{-/-}$ groups exhibited comparable SCE
179 burdens (p= 0.61) (**Fig. 3D**). Indicating that STING loss does not increase the instability
180 per cell but instead expands the proportion of cells that acquire elevated genomic
181 instability.

182 To assess whether SCEs preferentially occurred at specific genomic locations, such as
183 fragile sites or recombination hotspots, we mapped BPs genome-wide

using *Breakpoint.R* (*22*) and removed germline-associated BPs, defined as recurrent regions (>3 BPs per bin) detected in control cells (**Fig. 2E, fig. S3A-B**). Despite the significantly elevated SCE burden in *H2b*$^{\Delta IEC}$ and *H2b*$^{\Delta IEC}$/*STING*$^{-/-}$ cells, BPs were broadly distributed across the genome, indicating stochastic, genome-wide instability rather than localized fragility. Three notable enrichments were observed: two distinct peaks at the *H2b* locus on Chr14 (*H2b*$^{\Delta IEC}$ and *H2b*$^{\Delta IEC}$/*STING*$^{-/-}$) and at the *Sting (Tmem173)* locus on Chr18 (*H2b*$^{\Delta IEC}$/*STING*$^{-/-}$ only), likely reflecting rearrangements introduced during targeted gene deletion (**Fig. 3E, fig. S3, fig. S4**); and a third enriched region that corresponded to a subclonal inversion on Chr5 (Chr5:4,988,964-5,923,558). This inversion is unique to *H2b*$^{\Delta IEC}$/*STING*$^{-/-}$ cells and expanded to a cell fraction (CF) of 0.197 (n=12) (**Fig. 2E, fig. S4**), consistent with positive selection.

We next assessed whether STING loss induces structural chromosomal abnormalities, including aneuploidies, associated with oncogenic transformation. Both *H2b*$^{\Delta IEC}$ and *H2b*$^{\Delta IEC}$/*STING*$^{-/-}$ cells showed a marked increase in aneuploidy frequency compared to *H2b*$^{fl/fl}$ controls: 7.55% of *H2b*$^{fl/fl}$ cells possess aneuploidies, versus 35.8% in *H2b*$^{\Delta IEC}$ and 44.3% in *H2b*$^{\Delta IEC}$/*STING*$^{-/-}$ cells, corresponding to a 4.7-fold (p= 9.04e-05) and a 5.9-fold (p= 2.98e-06) increase, respectively (**Fig. 2F**). However, the difference between the two knockout populations was modest, and the overall number of aneuploidies per cell did not differ significantly between *H2b*$^{\Delta IEC}$/*STING*$^{-/-}$ and *H2b*$^{\Delta IEC}$ cells (p = 0.42) (**Fig. 2F-G**). These data indicate that STING loss does not substantially elevate whole-chromosome copy number changes beyond those induced by *H2b* deficiency alone. Integrating SCE burden with aneuploidy frequency, revealed a pronounced shift in the *H2b*$^{\Delta IEC}$/*STING*$^{-/-}$ population. Whereas the majority of *H2b*$^{\Delta IEC}$ cells remained genomically stable (58.2% in the low-BP/low-aneuploidy quadrant), *H2b*$^{\Delta IEC}$/*STING*$^{-/-}$ cells exhibited extensive genomic instability (67.2% in the high-BP/low-aneuploidy quadrant), with a marked increase in cells harbouring both high SCE levels and aneuploidies (22.9% vs 7.5% in *H2b*$^{\Delta IEC}$) (**Fig. 2H**).

Having learned that aneuploidies accumulate in both *H2b*$^{\Delta IEC}$ and *H2b*$^{\Delta IEC}$/*STING*$^{-/-}$ cells with only minor differences in overall frequency (1.2-fold, p= 0.335), we next investigated whether specific chromosomes were disproportionately affected. *H2b*$^{\Delta IEC}$/*STING*$^{-/-}$ cells displayed a significant enrichment of aneuploidies affecting chromosomes 14 (p= 0.021) and 15 (p= 0.00026) compared with *H2b*$^{\Delta IEC}$ cells (**Fig.**

216 **2I**). Chromosome 15 is of particular interest as it harbors key cancer-associated genes
217 such as *Myc* and *Rad21* and has been previously linked to tumorigenesis in mouse
218 models (*23*). Trisomy of Chr15 was detected in 14.8% of *H2b*$^{\Delta IEC}$/*STING*$^{-/-}$ cells and
219 arose independently in two distinct lineages (**Fig. 2J**). In "clone 1", a Chr5 inversion
220 (present in 19.7% of cells, as described above) preceded the gain of Chr15 (CF = 0.12),
221 followed by additional chromosomal alterations involving chromosomes 6, 12, and 14
222 (CF= 0.016, each). In "clone 2", Chr15 gain occurred independently (CF= 0.33), and
223 was followed by further alterations on chromosomes 6, 10, 14, and 19. The recurrent
224 and independent formation of Chr15 trisomies, together with their subsequent clonal
225 expansion and acquisition of additional aneuploidies in *H2b*$^{\Delta IEC}$/*STING*$^{-/-}$ cells,
226 suggests that loss of both *H2b* and *Sting* not only promotes aneuploidy but also creates
227 a permissive and selective environment for clonal evolution and ongoing chromosomal
228 alterations.

229 **STING deficiency impairs homologous recombination in intestinal epithelial cells**

230 The extensive chromosomal instability observed upon STING loss suggested a failure
231 of genome maintenance mechanisms. We therefore examined the extent to which
232 STING directly regulates DNA damage response (DDR) in IECs. Following induction
233 of DNA damage with AraC treatment, MODE-K WT cells exhibited a marked increased
234 γH2AX signal, but not in STING$^{-/-}$ cells (**Fig. 3A**), a finding that was further confirmed
235 by immunofluorescence staining (**fig. S8A-B**). Because γH2AX primarily reflects DNA
236 damage signaling and repair rather than DNA break formation per se (*24*), we next
237 assessed the amount of DNA breaks by performing comet assays. STING$^{-/-}$ cells
238 showed even higher levels of DNA damage after AraC treatment, compared to MODE-
239 K WT (**Fig. 3B-C**). Taken together, these results indicate that despite increased DSB
240 formation in STING$^{-/-}$ cells, STING deficiency results in impaired γH2AX induction.

241 Following DSB formation, HR repair is initiated by ATM dimer activation through
242 auto-phosphorylation at Ser1981, enabling phosphorylation of downstream DDR
243 targets such as H2AX (*25, 26*). To determine whether the reduced γH2AX signal
244 reflects impaired ATM activation, we assessed ATM phosphorylation and observed
245 markedly reduced p-ATM levels in MODE-K STING$^{-/-}$ cells compared to WT
246 following AraC treatment (**Fig. 3D**). To functionally validate defective HR repair, we

247 employed the DR-GFP reporter assay, which quantifies HR efficiency by measuring
248 restoration of functional GFP after I-SceI-endonuclease induced DSBs (*27*) (**Fig. 3E**).
249 Consistent with impaired ATM activation, STING deficiency resulted in significantly
250 reduced HR efficiency (**Fig. 3F**).

251 To determine whether this defective DDR requires the entire cGAS-STING pathway,
252 we repeated these experiments in MODE-K cGAS$^{-/-}$ cells. Similar to STING loss, cGAS
253 deficiency resulted in γH2AX induction (**fig. S8B-C**) and diminished ATM
254 phosphorylation (**fig. S8D**), despite comparable levels of DNA damage (**fig. S8E**).
255 These findings indicate that an intact cGAS-STING axis is required for efficient DNA
256 damage signaling in IECs.

257 We next investigated whether IFN-I, the canonical downstream effector of cGAS-
258 STING signaling (*28, 29*), mediates this DDR function. Notably, exogenous IFN-β
259 treatment failed to rescue γH2AX induction or ATM phosphorylation (**Fig. 3G**), and
260 knockdown of *Ifnar1* has no effect on DDR protein levels (**fig. S8F**). These results
261 indicate that cGAS-STING coordinates DDR independently of IFN-I signaling.

262 To further define the downstream pathway involved, we performed siRNA-mediated
263 knockdown of *Tbk1* and *Irf3*. *Tbk1* knockdown reduced ATM phosphorylation but did
264 not affect γH2AX induction, whereas *Irf3* knockdown had no detectable effect on either
265 parameter (**fig. S8G-H**), suggesting that cGAS-STING signaling contributes to DDR
266 initiation up to the level of TBK1 but independently of IRF3-mediated transcription.

267 We next explored the mechanism underlying ATM activation in MODE-K STING$^{-/-}$
268 cells. We first assessed WIP1 (PPM1D), a DDR phosphatase that promotes cell cycle
269 checkpoint termination by dephosphorylating multiple ATM pathway components (*30*).
270 Upon AraC treatment, WIP1 levels decreased in MODE-K WT cells but were increased
271 in both cGAS$^{-/-}$ and STING$^{-/-}$ cells, correlating with reduced p-ATM levels (**fig. S8I**).
272 However, siRNA-mediated knockdown of *Wip1* in STING$^{-/-}$ cells only partially
273 restored γH2AX levels and failed to rescue ATM phosphorylation, indicating that
274 aberrant WIP1 activity is not the primary cause of defective ATM activation in the
275 absence of STING (**fig. S8J**) (*30*).
276 Finally, we asked whether impaired ATM phosphorylation reflects defective ATM

recruitment to DNA damage sites. During HR, ATM is recruited to DSBs by the MRN (MRE11-RAD50-NBS1) complex, with NBS1 providing a critical C-terminal ATM-binding interface required for efficient ATM docking and activation (*31-33*). Consistent with this model, co-immunoprecipitation experiments revealed a markedly reduced interaction between NBS1 and ATM in MODE-K STING$^{-/-}$ cells compared with WT controls (**Fig. 3H**).

Collectively, these data demonstrate that STING loss compromises ATM-dependent DDR initiation by weakening NBS1-mediated ATM recruitment, while simultaneously altering DDR signal termination.

STING deficiency disrupts the G2/M checkpoint response in IECs

To identify the regulatory network underlying the STING-dependent DDR, we used MODE-K WT and STING$^{-/-}$ cells and performed kinase activity profiling using a PamGene assay to quantify phosphorylation dynamics of tyrosine kinases (PTKs) and serine/threonine kinases (STKs) kinases. STING loss was associated with a global reduction in both PTK and STK kinase activity under basal (untreated) conditions (**fig. S9A, B**). Following AraC-induced DNA damage, PTK activity was also globally reduced, whereas STK responses were heterogeneous, showing both increases and decreases (**fig. S9A-C**). Consistent with impaired IFN-I signaling, JAK1 and JAK2 activities were diminished. Similar trends were also found for several DNA damage-associated STKs, including IKKα, IKKβ, and ATR. In contrast, kinases linked to cell-cycle progression and proliferation, including CDK1, CDK7, and CDKL1, were upregulated in AraC-treated STING$^{-/-}$ cells. Among these, Cyclin-Dependent kinase 1 (CDK1) exhibited the strongest increase in kinase activity, based on kinase activity and phosphorylation status prediction (**Fig. 3I, fig. S9D-F**). Pathway enrichment analysis using EnrichR further revealed a significant downregulation of the p53 pathway in AraC-treated STING$^{-/-}$ cells (**fig. S9G**). The p53-p21 axis is a central regulator of the G2/M DNA damage checkpoint, acting to restrain CDK1 activity and prevent premature mitotic entry, whereas CDK1, a key Ser/Thr kinase, drives G2-to-M transition once checkpoint constraints are released (*34, 35*). To determine whether STING deficiency alters this checkpoint balance, we measured CDK1 and p21 levels in MODE-K cells after DNA damage. Consistent with the kinase screening results, STING$^{-/-}$ cells displayed elevated CDK1 phosphorylation and reduced p21 levels

309 confirming the attenuated p53 target genes such as *Mdm2* or *Ddit4l* (**Fig. 3J, fig. S10A-**
310 **B**). These data indicate that loss of STING impairs the p53-p21 arm of the DNA damage
311 response and shifts cells toward G2/M checkpoint failure. Notably, although cGAS
312 deficiency also impaired ATM activation, it did not reproduce the downstream
313 p21/CDK1 imbalance observed in STING-deficient cells, suggesting that this
314 checkpoint defect is selectively linked to STING (**Fig. 3J, fig. S10C-D**).

315 To determine whether these defects arise as an early, cell-intrinsic consequence of
316 STING loss rather than secondary effects of tumor progression or aging, we examined
317 DDR and G2/M checkpoint markers in intestinal crypts from young *H2b*$^{\Delta IEC}$/*STING*$^{-/-}$
318 and *H2b*/*STING*$^{\Delta IEC}$ mice prior to detectable tumor formation. Consistent with our
319 observations in MODE-K cells, both *H2b*$^{\Delta IEC}$/*STING*$^{-/-}$ mice and intestinal epithelium-
320 specific *H2b*/*STING*$^{\Delta IEC}$ mice displayed elevated CDK1 levels together with reduced
321 p21 and γH2AX in intestinal crypts compared with *H2b*$^{\Delta IEC}$ controls (**Fig. 3K**),
322 indicating a cell-autonomous defect in checkpoint control in vivo. Importantly, these
323 alterations persisted in aged *H2b*$^{\Delta IEC}$/*STING*$^{-/-}$ mice, which exhibited reduced ATM
324 phosphorylation and attenuated p53 signaling, further supporting impaired DDR
325 checkpoint enforcement upon epithelial STING loss (**Fig. 3L-N**).

326 **STING deficiency defines a chromosomal-instability-prone epithelial state**
327 **vulnerable to CDK inhibition**

328 Given the increased CDK1 activity and impaired genome maintenance observed above,
329 we asked whether STING-deficient tumors adopt a transcriptional program indicative
330 of CDK-driven proliferation. RNA sequencing of intestinal organoids derived from
331 *H2b*$^{\Delta IEC}$ and *H2b*$^{\Delta IEC}$/*STING*$^{-/-}$ mice revealed distinct global transcriptomic profiles
332 between the two genotypes (**Fig. 4A-C**).

333 In addition to the downregulation of interferon signaling and host immune defense
334 pathways, gene ontology analysis revealed a marked reduction in chromosome
335 segregation and mitotic spindle organization signatures in *H2b*$^{\Delta IEC}$/*STING*$^{-/-}$ organoids
336 (**Fig. 4D**). To quantify this finding, we calculated a chromosome segregation signature
337 score and found it markedly reduced in *H2b*$^{\Delta IEC}$/*STING*$^{-/-}$ organoids (**Fig. 4E**),
338 suggesting disrupted mitotic fidelity, which may underlie the observed aneuploidy

339 accumulation.

340 Transcription factor activity analysis further revealed substantial rewiring of regulatory
341 networks in *H2b*$^{\Delta IEC}$/*STING*$^{-/-}$ organoids. Regulons associated with TRIM28, SP1, and
342 EN1 were enriched, whereas those linked to HNF4A and ETV4 were reduced (**Fig. 4F**),
343 indicating altered transcriptional control of epithelial identity and cell-cycle-related
344 processes. Collectively, these changes suggest a transcriptional state compatible with
345 dysregulated proliferation and genome maintenance.

346 These transcriptional changes suggested that STING-deficient tumors may rely on
347 CDK-driven mitotic progression. We therefore tested the effects of pharmacological
348 CDK inhibition. Firstly, we examined CDK1 expression in tumors and found all tumor
349 samples derived from both *H2b*$^{\Delta IEC}$/*STING*$^{-/-}$ mouse (n=5) and *H2b*/*STING*$^{\Delta IEC}$ mouse
350 (n=3) were positive for CDK1 (**Fig. 4G-H, fig. S11A-B**). Subsequently, organoids
351 established from these tumors exhibited complete loss of proliferative capacity upon
352 treatment with the pan-CDK inhibitor AZD5438 (**Fig. 4I-J, fig. S11C-D**). Based on the
353 STING-CDK1 signature, we asked whether STING expression governs the sensitivity
354 of tumor cells towards CDK inhibitor. In MODE-K cells, STING$^{-/-}$ cells were
355 significantly more sensitive than WT or cGAS$^{-/-}$ controls (**fig. S12A**). We further
356 compared the IC_{50} values in murine tumor organoids from *H2b*$^{\Delta IEC}$/*STING*$^{-/-}$ mice with
357 murine tumor organoids harboring *Kras*^{G12D} or *Braf*^{V637E} mutations and confirmed
358 STING-genotype specific sensitivity to CDK inhibition (**Fig. 4K, fig. S12B-F**).
359 Extending these findings to human disease, we tested AZD5438 across multiple human
360 adenocarcinoma cell lines in which STING deficiency has been systematically assessed
361 previously. We observed that the sensitivity was inversely correlated with STING
362 expression levels, indicating that reduced STING expression predicts enhanced
363 responsiveness to CDK inhibition (*16*) (**Fig. 4L, fig. S12G-O**). Collectively, these
364 results identify defective STING-mediated DDR as a key driver of hyperproliferation
365 and chromosomal instability and uncover CDK inhibition as a potential therapeutic
366 vulnerability in STING-deficient tumors.

367 **Discussion**

368 While the mechanistic concept of DNA damage, cytosolic dsDNA accumulation and

369 cGAS-STING dependent sensing is widely established across several species and cell
370 types, the immediate role of the cGAS-STING pathway on preserving genome integrity
371 has remained inconclusive (*36-39*). Here, we challenge the prevailing view of STING
372 as primarily an immunostimulatory sensor and reposition STING as an epithelial, IFN-
373 I-independent regulator upstream of HR.

374 Using *H2b*$^{\Delta IEC}$/*STING*$^{-/-}$ mice model, we show that these mice develop spontaneous
375 intestinal adenocarcinoma and further transform into metastatic tumors.
376 Mechanistically, we show that cGAS/STING deficiency reduces the interaction
377 between ATM and NBS1, a central component of the MRN complex, thereby
378 attenuating ATM recruitment and activation. This finding underscores a critical role for
379 the cGAS/STING axis in initiating DSB-induced DDR. In parallel, loss of
380 cGAS/STING enhanced γH2AX dephosphorylation through upregulation of the
381 phosphatase WIP1, further compromising DNA damage signaling. Together, these
382 findings reveal a dual function of cGAS-STING in coordinating both the activation and
383 maintenance of DDR.

384 To explicitly resolve the consequence of defective STING on genome integrity, we
385 employed Strand-seq and RNA-seq. Our data revealed that double deficiency of H2b
386 and STING may induce extensive sister chromatid exchanges and chromosome-
387 specific aneuploidies, e.g. trisomy 15, which harbors oncogenic drivers such as *Myc*
388 and *Rad21*. These genomic alterations coincide with downregulation of chromosome
389 segregation and mitotic spindle genes, and reprogramming of transcription factors
390 including TRIM28, SP1, and EN1, indicating a shift toward a dedifferentiated, DNA
391 damage-tolerant state. Importantly, this transcriptional reprogramming was
392 accompanied by elevated CDK activity and impaired G2/M checkpoint control,
393 consistent with a hyperproliferative phenotype. Together, these findings delineate a
394 mechanistic cascade whereby defective DNA repair and cell-cycle control synergize to
395 promote chromosomal instability, clonal selection and tumor evolution.

396 We wondered whether the very same properties that promote STING-dependent tumor
397 formation may also generate a mechanistic vulnerability that can be targeted
398 therapeutically. We could demonstrate that STING-deficiency results in increased
399 CDK1 activation. Importantly, we observed a striking dichotomy between STING and

400 cGAS, as cGAS deficient cells retained functional p53 signaling.

401 Notably, CDK inhibition effectively suppresses the growth of H2b/STING-deficient
402 organoids and tumors, establishing aberrant CDK signaling as a critical vulnerability in
403 this context. Extending these findings to human cancer models, STING-low
404 adenocarcinoma cell lines displayed heightened sensitivity to CDK inhibition,
405 suggesting that defective STING-mediated DNA damage response dictates both
406 proliferative drive and therapeutic susceptibility. Our findings have fundamental
407 implications. First, while pan-CDK inhibitors have been hindered by dose-limiting
408 toxicity (*40*), our data suggest that the intrinsic CDK dependency of STING-deficient
409 tumors transforms this toxicity challenge into a dosage-selectivity opportunity (*15, 41*).
410 Potential limitations might be the fact that single-strand seq was conducted in
411 *H2b*$^{\Delta IEC}$/*STING*$^{-/-}$ but not in *H2b*/*STING*$^{\Delta IEC}$. However, we point out that tumor
412 manifestation incidence and CDK1 activation was comparable in both genetic models,
413 arguing for an epithelial-cell intrinsic function of STING.

414 Our results not only provide a mechanistic rationale for targeting CDK pathways in
415 STING-deficient intestinal tumors but also highlight a broader principle in which loss
416 of genome maintenance reprograms cell-cycle control to fuel oncogenic adaptation.
417

418 **Materials and Methods**

419 **Cell culture**

420 Mouse intestine epithelial cell line MODE-K (WT and Knock out) was cultured in DMEM
421 GlutaMAX-I (Gibco, #61965-026) medium containing 10% fetal bovine serum (Sigma,
422 #F7524), 1% HEPES 1M (Gibco, #15630-056), 1% NEAA 100x (Gibco, #11140-035)
423 and 1% penicillin streptomycin (Gibco, #15140-122) at 37℃ in a constant temperature
424 incubator with 5% CO2.

425

426 **Generating of MODE-K cGAS$^{-/-}$ and STING$^{-/-}$ cell line by using Crispr-Cas9 system**

427 Single-stranded DNA with guiding sequence target for mice *cGAS* (Fw 5′-
428 AGATCCGCGTAGAAGGACGAGTTTT-3′; Rev 3′-
429 TCGTCCTTCTACGCGGATCTCGGTG-5′) and *Tmem173* gene (Fw 5'-
430 CAGTAGTCCAAGTTCGTGCGGTTTT-3', Rev 5'-
431 CGCACGAACTTGGACTACTGCGGTG-3') were annealed and cloned into CRISPR
432 nuclease vector via GeneArt® CRISPR Nuclease Vector with OFP Reporter Kit
433 （Thermofisher, A21174）. Vector with target sequence were then transformed into
434 TOP 10 competent *E. coli* (Thermofisher, C404003) and selected via ampicillin LB solid
435 medium. The selected bacteria were then enriched and proceeded with plasmid
436 extraction by using HiSpeed Plasmid Midi Kit (Qiagen, 12643) for further transfection.
437 MODE-K WT cells were seeded one day before transfection, and transfected purified
438 plasmid DNA into the cells on the next day by using Lipofectamine™ 3000 Reagent
439 (Thermofisher, L3000015), and incubated in 37℃, 5% CO2 incubator overnight. After
440 24h of incubation, cells transfected with CD4 reporter vector were enriched and
441 selected by CD4 Dynabeads. Selected cells then diluted and seeded into 96 well plates
442 with 1 cell each well. After cultured for 7-14 days, cells with single colony were selected
443 out, those cells were enrichment cultured and further tested by Western Blot.

444

445 **Immunofluorescence for cells**

446 Cells were seeded onto autoclaved coverslips within a cell culture plate. Following the
447 desired stimulation or transfection, the cells were fixed and permeabilized using -20°C
448 methanol for 10 minutes at room temperature. After washing with PBS, the cells were
449 blocked using 2% BSA solution for 1 hour. Subsequently, the cells were subjected to
450 overnight incubation at 4°C with the primary antibody (**table S1**). The next day, after

451 washing away unbound primary antibody, the cells were incubated with the appropriate
452 secondary antibody (**table S1**) for 1 hour at room temperature while protecting them
453 from light. Additional washing steps with PBS were performed to remove excess
454 secondary antibody. To visualize the nuclei, the cells were stained with a fluorescent
455 nuclear dye such as DAPI or Draq5, and then a final wash with PBS was carried out.
456 Finally, the coverslips were mounted onto microscope slides for microscopy.
457
458 **Gene expression Taqman assay**
459 Total RNA was isolated from all biopsies and samples (cells, organoids, and mouse
460 tissues) using the RNeasy Kit (Qiagen, #74106) according to the manufacturer's
461 instructions. First-strand cDNA was synthesized using the Maxima H Minus First
462 Strand cDNA Synthesis Kit (Thermo Fisher Scientific, #K1652) following the
463 manufacturer's protocol. Quantitative PCR was performed using TaqMan Gene
464 Expression Assays (**table S2**). Reactions (10 μL total volume) contained 5 μL cDNA (2
465 ng/μL) and 5 μL TaqMan Master Mix supplemented with 0.5 μL TaqMan assay
466 primer/probe and 4.5 μL mix, and were run on a Roche real-time PCR system
467 (LightCycler® 96 Instrument, Roche). Relative gene expression was calculated using
468 ***β-actin*** (*Actb*) as the endogenous reference gene.
469
470 **Western blot**
471 Cell lysates were extracted and prepared in RIPA buffer (Thermofisher, #89901)
472 containing 1% Phosphatase Inhibitor Cocktail (Sigma, # P5726). The concentration of
473 protein was measured by lowry assay (Biorad, #5000116). Equal amounts of proteins
474 (15-20μg) were loaded and separated by SDS-PAGE gel, then transferred onto PVDF
475 membrane (BIO-RAD, # 162-0177). The membranes were blocked by 5% non-fat milk
476 (Santa-Cruz, # sc-2325) in TBST for 1h and incubated with specific primary antibody
477 (**table S1**) overnight in 4℃ or 1h in room temperature. Subsequently, the membranes
478 were incubated with HRP-coupled secondary antibody (**table S1**) for 1h in room
479 temperature and developed by ChemiDocTM imaging system (Biorad, #12003263)
480 with ECL reagent (Biorad, #1705062).
481
482 **Cell IC_{50} analysis**
483 IC_{50} values for AZD5438 were determined using CellTiter-Glo-based viability assay

484 （Promega, #G9042） in 96-well format. Cells were seeded at 1.2 × 10^4 cells per well
485 in white 96-well plates in 100 μL complete medium. After 24 h, the medium was
486 replaced with fresh medium containing a serial dilution of AZD5438, and cells were
487 incubated for an additional 72 h. CellTiter-Glo reagent (100 μL) was then added directly
488 to each well, followed by incubation for 20 min at room temperature. For cell cultured
489 in transparent plate, remove the medium and add 100 μL CellTiter-Glo reagent and
490 transfer to a white 96-well plate after 20min incubation. Luminescence was measured
491 using a microplate reader. Dose-response curves and IC50 values were calculated in
492 GraphPad Prism using nonlinear regression.
493
494 **Co-Immunoprecipitation**
495 Cells were lysed in NP-40 lysis buffer containing 1% protease inhibitor on ice for 30
496 min, followed by centrifugation at 12,000 × g for 10 min at 4 °C. Protein concentrations
497 were determined by standard assays. Equal amounts (200-500 ng) of total protein
498 were incubated with primary antibody (1:100) **(table S1)** or species-matched IgG as a
499 negative control overnight at 4 °C. Magnetic beads (30 μL per sample) were washed
500 three times with NP-40 lysis buffer and blocked with 2% BSA for 30 min on ice, then
501 added to the protein-antibody mixtures and incubated for 4h at 4 °C. Beads were
502 collected using a magnetic rack, washed three times with NP-40 lysis buffer, and
503 proteins were eluted in 30 μL of 1× SDS loading buffer by heating at 95 °C for 5 min.
504 10% of total lysate was used as input. Samples were analyzed by SDS-PAGE followed
505 by western blotting.
506
507 **Comet assay**
508 MODE-K cells were seeded in 6-well plates and treated with either PBS (vehicle control)
509 or 2.5 μM cytarabine (AraC) (Sigma-Aldrich, C6645) for 20 h. Cells were then
510 harvested, and viable cell numbers were determined using an automated cell counter
511 (LUNA II, Logos Biosystems) prior to comet assay analysis. DNA damage was
512 quantified using an alkaline comet assay (Comet Assay® Kit, 4250-050-ESK; R&D
513 Systems) according to the manufacturer's instructions. Briefly, low-melting-point
514 agarose (LMA) was melted at 90 °C and equilibrated to 37 °C. Cells were mixed with
515 LMA, and 100 μL of the suspension was applied to CometSlides and spread evenly.
516 Agarose gels were allowed to solidify at 4 °C for 10 min. Slides were then incubated in

517 lysis buffer at 4 °C overnight. Following lysis, DNA was unwound in alkaline unwinding
518 solution for 20 min. Electrophoresis was performed in alkaline running buffer at 21 V
519 for 30 min at 4 °C. Slides were washed twice with deionized water and once with 70%
520 ethanol, then stained with SYBR Gold (Invitrogen, S1194) for 10 min in the dark. After
521 rinsing with deionized water and drying at 37 °C, comets were imaged using an ECHO
522 microscope and comet tail length was quantified.
523
524 **Protein kinase assay**
525 MODE-K WT and STING$^{-/-}$ cells after treated with control (PBS) or 2.5 µM AraC
526 (Siggma-Aldrich, C6645) for 20h were lysed based on the manufacturers protocol
527 (PamGene Protocol 1160) with 100 µL MPer (Thermo Scientific) spiked with 1:100
528 Halt® Phosphatase-Inhibitor-Cocktail (Thermo Scientific) and 1:100 EDTA-free Halt®
529 Protease-Inhibitor-Cocktail (Thermo Scientific). Protein concentrations of the samples
530 were evaluated with Lowry assay.
531 Kinase activity profiling was performed with Tyrosine Kinase and Serine-Threonine
532 Kinase PamChip-4® Arrays (PamGene) using a PamStation® 12. Each chip has four
533 arrays and the array´s surface consists of porous silica with 196 (PTK) or 144 (STK)
534 distinct peptide targets, composed of 13 amino acids mimicking phosphorylation sites,
535 that are printed in spots on the porous silica surface. For the tyrosine kinase analysis,
536 a FITC-conjugated antibody was used to quantify the phosphorylation level.
537 Furthermore, the kinetic of the reaction was measured by pumping the sample fluid
538 through the porous surface for 94 cycles. From cycle 37 to 92 every five cycles and at
539 cycle 94 five pictures each with different exposure times (10 ms, 20 ms, 50 ms, 100
540 ms and 200 ms) were taken. For the serine-threonine kinase analysis, a primary
541 antibody was used and after cycle 90 a secondary FITC-antibody against the primary
542 antibody was given on the arrays for quantification. From cycle 92 to 122 every five
543 cycles and after cycle 124 five pictures each with different exposure times (10 ms, 20
544 ms, 50 ms, 100 ms and 200 ms) were taken. The brightness of each spot was
545 measured against reference spots and used for further analysis. The kinase activity
546 profiling was performed using 2 biological replicates distributed each on different chips
547 and arrays with 5 µg (PTK) or 1 µg (STK) protein per array and a final concentration
548 of 400 µM ATP according to the manufacturers protocol. BioNavigator® 6 (PamGene)
549 was used for signal evaluation and upstream kinase analysis following the

550 manufacturers protocol. Data from the upstream kinase analysis was integrated into
551 EnrichR. Threshold cut-off for the median finale score was made at 1,2 or 1,0,
552 respectively, and median kinase statistic results arranged from up to down before
553 converting the UniPROT IDs from the main kinases with lower activity into gene names
554 using UniProt. Gene names were pasted into EnrichR to draw a connection between
555 the genes and their corresponding pathways.
556
557 **DR-GFP HR reporter assay**
558 MODE-K WT and STING$^{-/-}$ cells were seeded into 24-well plates in triplicate and
559 cultured in serum-free medium. Cells were transiently transfected with the DR-GFP
560 reporter plasmid (Addgene, #26475) using LipofectamineTM 3000 Reagent
561 (Thermofisher, L3000015) according to the manufacturer's instructions. After 24 h,
562 cells were re-transfected with DR-GFP together with the I-SceI expression plasmid
563 (Addgene, #26477) to induce site-specific DSBs. 48 hours after the second
564 transfection, cells were harvested, and GFP-positive cells were quantified by flow
565 cytometry (SONY FACS SA3800) DSB repair efficiency was calculated based on the
566 percentage of GFP-positive cells as described previously.
567
568 **Generating of knockout mice**
569 Epithelial deficiency of *Rnaseh2b* (*H2b*$^{\Delta IEC}$) mice were generated as described
570 previously (*3*). Mouse with full-body deficiency of *Tmem173* (*STING*$^{-/-}$) were generated
571 by Crispr/Cas9 system while *STING*$^{fl/fl}$ mice were obtained from the Jackson
572 Laboratory (#:031670) to generate intestinal epithelial specific deficiency of *Tmem173*.
573 *STING*$^{-/-}$ and *STING*$^{\Delta IEC}$ mice were paired with *H2b*$^{\Delta IEC}$ mice to generate
574 *H2b*$^{\Delta IEC}$/*STING*$^{-/-}$ and *H2b*/*STING*$^{\Delta IEC}$ respectably. All mice were housed in a specific
575 pathogen-free (SPF) animal facility at Kiel University under standard conditions, with
576 ad libitum access to food and water and a 12 h light/dark cycle. Age-matched female
577 and male mice were used for all experiments. Animal experiments with basal
578 phenotype were performed in accordance guidelines with Kiel University (animal vote
579 IX 552-241316/2022).
580
581 **Tissue processing**
582 Mouse small intestine and colon were cut and opened longitudinally, then followed by

583 Swiss rolling from the distal to proximal part. All the mouse tissue was fixed by 10%(w/v)
584 formalin for 24h at 4°C. Fixed tissues were embedded in paraffin blocks and were cut
585 for H&E and IHC staining according to the method described before (*42*).
586
587 **H&E stanning**
588 Paraffin-embedded tissue sections were dewaxed in xylene substitute (Roti-Histol;
589 Carl Roth) for 10 min, rehydrated through graded ethanol (3 × 1 min in 100%, 2 × 1
590 min in 96%, 1 × 1 min in 70%), and washed in distilled water for 5 min with one solution
591 change on a shaker. Sections were stained with Mayer's hematoxylin solution
592 (Hämalaun sauer nach Meyer; Carl Roth) for 3 min (without shaking), rinsed under
593 running tap water for 5 min for bluing, and counterstained with 0.1% aqueous eosin G
594 (prepared by dilution from 1% stock; Carl Roth) for 3 min, followed by a 30 s rinse
595 under running tap water. Slides were dehydrated in ascending ethanol (10 dips in 70%,
596 3 × 10 dips in 96%, 2 × 10 dips in 100%, then 3 × 2 min in 100%), cleared in xylene
597 substitute (10 dips in the first bath, then 2 × 2 min in fresh baths), and mounted with
598 Roti-Histokitt (Carl Roth); mounted slides were left to evaporate/dry for at least 24 h
599 before further handling. Tumor classification on H&E-stained sections was performed
600 by a pathologist according to the latest WHO Classification of Tumors of the Digestive
601 System (*43*).
602
603 **DAB staining**
604 Paraffin-embedded sections were dewaxed in xylene substitute (Roti-Histol; Carl Roth,
605 #6640.2) for 10 min, rehydrated through graded ethanol (3 × 60 s in 100%, 1 × 60 s in
606 96%, 1 × 60 s in 70%), and rinsed briefly in distilled water, followed by PBS washes (3
607 × 4 min). Antigen retrieval was performed in citrate buffer (10 mM citric acid, pH 6) by
608 heating in a pressure cooker for 20 min, then sections were washed again in PBS (3
609 × 4 min). Endogenous peroxidase activity was quenched with 3% H_2O_2 for 10 min,
610 followed by PBS washes (3 × 4 min). Sections were blocked for 30 min with 1% BSA
611 in PBS containing 0.2% Triton X-100, excess solution was removed, and primary
612 antibodies (**table S1**) diluted in 1% BSA/PBS were incubated overnight at 4°C in a
613 humidified chamber. After PBS washes (3 × 4 min), sections were incubated with
614 biotinylated secondary antibodies (**table S1**) for 45 min, washed in PBS (3 × 4 min),
615 and incubated with VECTASTAIN Elite ABC reagent for 45 min. After PBS washes (3

616 × 4 min), signal was developed using a DAB peroxidase substrate solution (Vector SK-
617 4100; prepared in 5 mL distilled water with buffer, DAB, and peroxidase) until the
618 desired staining intensity was reached, then rinsed in distilled water (5 min). Sections
619 were counterstained with Mayer's hematoxylin for 1 min and blued under running tap
620 water for 5 min, dehydrated in ascending ethanol (70%, 96%, 100%), cleared in xylene
621 substitute, and coverslipped.
622
623 **Immunofluorescence for mouse tissue**
624 Deparaffinization, rehydration, and heat-induced antigen retrieval were performed as
625 described for the DAB staining protocol above. After antigen retrieval, sections were
626 then blocked for 30 min in 5% BSA in PBS containing 0.2% Triton X-100, incubated
627 with primary antibodies (**table S1**) diluted in 1% BSA/PBS overnight at 4°C, and
628 subsequently incubated with Alexa Fluor-conjugated secondary antibodies (1:500, 45
629 min, dark) (**table S1**). Nuclei were counterstained with DAPI (1:40,000 in PBS, 10 min,
630 dark), followed by PBS washes, and slides were mounted with fluorescence mounting
631 medium and stored at 4°C. The prepared slides were proceeded to microscopy and
632 images were acquired using a Zeiss AxioImager.Z1 microscope equipped with
633 Apotome and AxioVision Rel. 4.9 software (ZEISS, Oberkochen, Germany).
634
635 **Organoid Isolation**
636 Mice were euthanatized according to animal care of the Christian-Albrechts-University
637 (Kiel, Germany), and separate ileum out from small intestine. Remove fat as much as
638 possible and washed by cold PBS. Cut the ileum longitudinally and cut them into 5mm
639 small pieces after washed by cold PBS to remove the mucus and feces. Incubate these
640 ileum spices in 5mM ice cold EDTA for 10min then shaking intermittently, the discard
641 the supernatant which containing villus and repeat this step for 3 times. Discard
642 supernatant and replaced by cold PBS then shake for 30s and incubate for 5min,
643 repeat this step for 3 times. Screen the supernatant through a 100nm cell strainer and
644 spin down with 400g for 5min in 4℃. Resuspend the pellet with Advanced DMEM F12,
645 after counted by microscope, seed the crypts into cell culture plate with Matrigel and
646 cultured with conditional hEGF-Noggin-Rspondin (ENR) medium.
647
648 **Organoid Passage**

649 Discard the old medium and remove the Matrigel containing organoids with cold PBS
650 into a 15ml falcon, then pipette it up and down to break organoids. Spin down by and
651 discard the supernatant, and seed organoids with Matrigel to a cell culture plate, then
652 place the plate into 37℃ an incubator for 20 to 40min. After the Matrigel became hard,
653 add ENR medium.
654
655 **Organoid IC_{50} analysis**
656 Organoid viability and IC_{50} were determined in tumor-derived organoids. Organoids
657 were dissociated with TrypLE Express (Gibco, Thermo Fisher Scientific) into single
658 cells or small clusters, resuspended in Matrigel, and seeded in triplicate using pooled
659 material from 3-4 confluent wells of a 24-well plate for six drug concentrations. Seeding
660 density was adjusted visually under brightfield microscopy to ensure comparable
661 density across conditions, and Matrigel was mixed thoroughly during dispensing to
662 minimize uneven distribution. After seeding, organoids were cultured overnight in ENR
663 medium supplemented with Y-27632 (abcam, ab120129). On the following day (Day
664 0), organoids were treated with increasing concentrations of AZD5438 (0.008, 0.04,
665 0.2, 1, 5, and 20 μM) or vehicle control. After 72 h of treatment, cell viability was
666 assessed using the CellTiter-Glo assay according to the manufacturer's instructions.
667 Luminescence was measured following transfer to a white 96-well plate, and
668 normalized viability values were used to calculate IC_{50} using GraphPad Prism.
669
670 **Organoid colony forming assay**
671 Organoid colony-forming assay was performed by dissociating organoids into single
672 cells using TrypLE Express (Gibco, Thermo Fisher Scientific). A total of 10,000 cells
673 were embedded in Matrigel and cultured in ENR medium supplemented with Y-27632
674 (abcam, ab120129), with medium changed every other day. Stimulants were added on
675 Day 2 as indicated. On Day 3, medium was replaced with standard ENR without Y-
676 27632. Colony formation was assessed on Day 7 by colony counting or by measuring
677 viability using the CellTiter-Glo assay.
678
679 **Orthotopic organoid transplantation**
680 Orthotopic transplantation was performed using two independent organoid lines
681 derived from two individual mice and carried out according to previous description (*4*).

682 Each organoid line was transplanted into four recipient immunocompromised NSG
683 (NOD.Cg-Prkdcscid Il2rgtm1Wjl/SzJ, Stock No: 005557) mice which were purchased
684 from Charles River Laboratories (Research Models and Services, Germany GmbH,
685 Sulzfeld, Baden-Württemberg, Germany) and housed, bred and maintained in SPF
686 facilities (ZPF, TUM University Hospital, Technical University of Munich, Germany).
687 Orthotopic organoid transplantation was performed as previously described (*44, 45*).
688 Briefly, prior to transplantation, organoids were dissociated to generate small clusters
689 (approximately 5-10 cells) using TrypLE Express (Gibco, Thermo Fisher Scientific) and
690 suspended in a reduced-volume injection medium composed of Advanced DMEM/F12
691 supplemented with B27 (1×), N2 (1×), L-glutamine (Gibco, Thermo Fisher Scientific),
692 10% (v/v) Matrigel (Corning), 1% (v/v) penicillin/streptomycin, and 10 μM Y-27632
693 (STEMCELL Technologies). For each injection, 50 organoid clusters were prepared in
694 a total volume of 100 μL while each mouse was administered 2-3 injections. Recipient
695 mice were anesthetized, and the colonic lumen was gently flushed with PBS using a
696 syringe fitted with a straight gavage needle. Endoscopy-guided delivery was performed
697 with a rigid mini-endoscope system (Karl STORZ; 1.9 mm diameter; ColoView).
698 Organoid suspensions were deposited into the colonic submucosa using a flexible 33G
699 needle (Hamilton; custom 16-inch length; 45° bevel). Orthotopic tumor formation and
700 metastatic lesions were subsequently assessed, then proceed with H&E staining and
701 microscopy analysis. Data were analyzed using GraphPad Prism. The animal studies
702 were conducted in compliance with European guidelines for the care and use of
703 laboratory animals and were institutionally approved by the Institutional Animal Care
704 and Use Committees (IACUC) of Technical University of Munich and by the District
705 Government of Upper Bavaria.
706
707 **Strand Sequencing (Strand-seq)**
708 Strand-seq library preparation: Small intestine organoids were isolated from an aged
709 mouse (>53W, n=1) and cultured using ENR medium as described above. After
710 passaging (P1), organoids were left to grow for 4 days before Bromodeoxyuridine
711 (BrdU; Sigma, B9285; 40 μM) was added to the culture media for 8, 12 or 16h (as
712 shown in fig. S7). The organoids were then dissociated into single cells using TrepLE
713 Express (#12604021) and stored at -80°C in freezing media containing 10% DMSO
714 and 90% FBS. To sort BrdU+ cells, the samples were thawed at 37°C, and washed

715 once by adding 4 ml of 0.01% BSA (Thermofisher,15260037) in 1X PBS (Sigma,
716 882114) and centrifuged at 500g for 5 minutes. The supernatant was then decanted
717 and the cells were resuspended in 200µl of nuclei staining buffer (100 mM Tris-HCl
718 pH7.4, 154 mM NaCl, 1 mM CaCl2, 0.5 mM MgCl2, 0.2% BSA, 0.1% NP-40, ultra pure
719 water, 10 ug/ml Hoechst 33258, 10 ug/ml PI) as described in previous publications (*22*).
720 Single nuclei from the appropriate time point of BrdU (fig. S9) were sorted using the
721 cell sorter BD FACSAria Fusion, in 96-well plates containing 5µl of freshly prepared
722 Freeze buffer (ProFreeze_CDM (2X), 100% DMSO, 1X PBS). The plates were stored
723 at -80°C until library preparation was performed, as described previously (*22*).
724 Libraries were sequenced on an Illumina NovaSeq X Plus sequencing platform using
725 pair-end sequencing protocol (75-bp), demultiplexed and aligned to the mouse
726 reference genome (mm09).
727 Strand-seq analyses, breakpoint and aneuploidies counts: High quality libraries,
728 obtained from cells that incorporated BrdU for one complete round of DNA replication,
729 were selected as described previously (*22*). Sharp changes in read alignment
730 directionality (for example from WC to CC), or breakpoints, were identified and
731 quantified in two different ways: 1. Manually counting somatic breakpoints for each cell.
732 2. Using the computational tool BreakpointR, with a 2 Mb window-size parameter, to
733 determine the genomic coordinates of the confidence interval for each breakpoint. The
734 mouse genome was binned into 500 kb intervals, and breakpoint counts were
735 quantified per bin. A cutoff of 3 breakpoints per bin in the *H2b*$^{fl/fl}$ (WT) condition was
736 applied, and bins meeting this criterion were classified as putative “germline” mutation
737 regions. For a specific region on chromosome X (chrX:25,500,000-35,000,000), the
738 boundaries were manually adjusted due to a highly segmented duplicated locus in the
739 reference genome that inflated breakpoint counts. The resulting set of genomic regions
740 was then used to filter breakpoints in *H2b*$^{fl/fl}$, *H2b*$^{\Delta IEC}$ and *H2b*$^{\Delta IEC}$ /*STING*$^{-/-}$ cells.
741 The aneuploidies were identified in the Strand-seq libraries by manually investigating
742 the high-quality libraries. Specifically, changes in mean read depth were identified
743 across large genomic regions, including whole-chromosome events, chromosome-
744 arm-level alterations, and partial copy-number losses or gains exceeding 5 Mb. In
745 Strand-seq data, aneuploidy can be inferred from strand-state imbalances by
746 quantifying the Watson-to-Crick read ratio along the genome. Deviations from the
747 expected ~1:1 ratio indicate copy-number changes; for example, a Watson-specific

748 gain is reflected by an increased Watson fraction, yielding an approximate
749 Crick:Watson ratio of 1:2 across the affected region.
750
751 **RNA Sequencing (RNA-seq)**
752 Total RNA was isolated from *H2b*$^{\Delta IEC}$ and *H2b*$^{\Delta IEC}$ /*STING*$^{-/-}$ mouse organoids (n = 2
753 mice; three replicates per mouse) using the QIAGEN RNeasy Kit according to the
754 manufacturer's instructions. Samples were sequenced on HiSeq3000 (Illumina, San
755 Diego, United States) using Illumina total RNA stranded TruSeq protocol. An average
756 of ~40 million 75-nt paired-end reads was sequenced for each sample. Raw reads
757 were pre- processed using cutadapt (*46*) to remove adapter and low-quality sequences.
758 RNAseq reads were aligned to the human genome (GrCh38) reference genome with
759 TopHat2 (*47*). Gene expression values of the transcripts were computed by HTSe (*48*).
760 Differential gene expression levels were analysed and visualized by the Bioconductor
761 package DESeq2 (*49*). DeSeq2 was used to perform principal component analysis
762 (PCA) that illustrate a separation according to the first principal component between
763 different treatments. Venn diagrams were drawn using Venn Diagram package in R.
764 Gene Ontology (GO) terms were obtained within the category of biological processes
765 using the Innate DB database (www.innatedb.com) (*50*). Differential expression of
766 genes between each treatment type versus control samples was determined using
767 Wald tests to calculate the significance of differential expression for each gene in a
768 pair-wise comparison between treatment types versus control.
769
770 **Statistics and reproducibility**
771 Statistical analyses were performed using GraphPad Prism, and data are presented
772 as mean ± SEM. Data distribution was first assessed using the Shapiro-Wilk normality
773 test. For comparisons between two groups, an unpaired two-tailed Student's t-test was
774 applied when data followed a normal distribution; otherwise, the nonparametric Mann-
775 Whitney U test was used. All statistical tests were two-sided, and p values < 0.05 were
776 considered statistically significant. Additional statistical details are provided in the
777 figure legends.

778

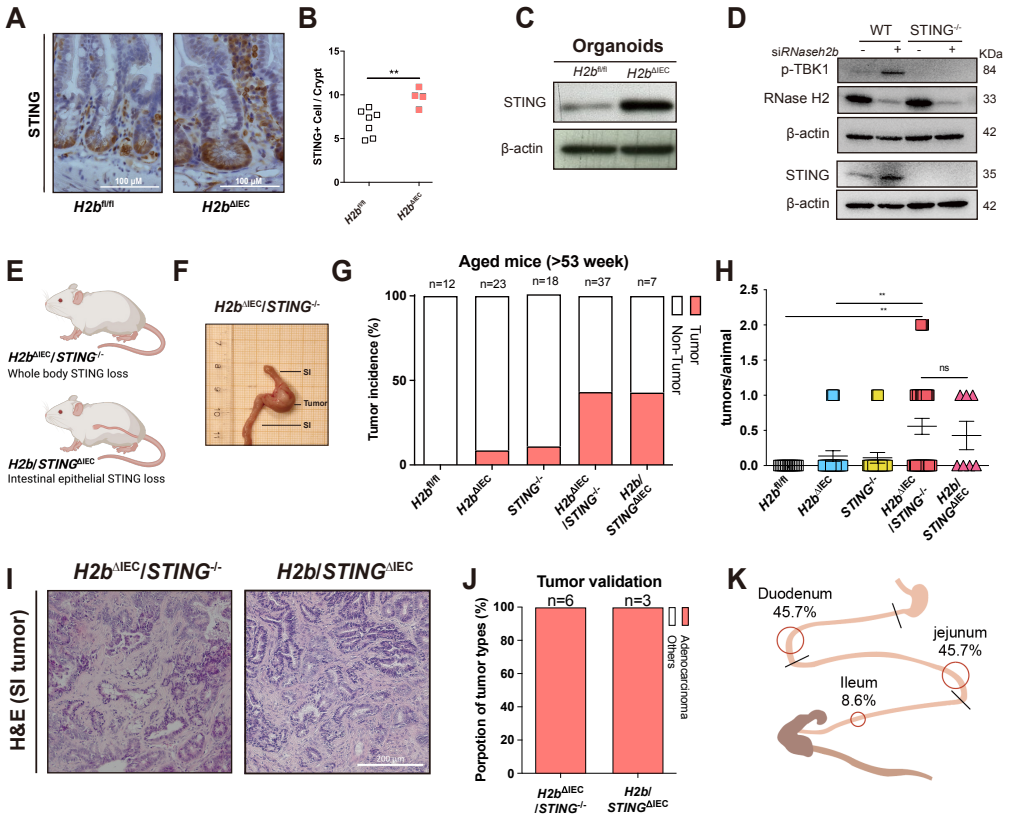

Fig. 1. Loss of STING promotes intestinal tumorigenesis and progression in the context of epithelial DNA damage

(A and **B)** Immunohistochemical staining (**A**) and statistical analysis (**B**) of STING staining in the small intestine of 8-12 week old *H2b*$^{fl/fl}$, (n=7), *H2b*$^{\Delta IEC}$ (n=4) mice. The average number of STING-positive cells per crypt was determined by counting ≥30 crypts per sample, and the mean number of positive cells per crypt was calculated. Significance was determined using unpaired two-tailed Student's test.

(C) Western Blot analysis of STING in small intestinal organoids from 8-12 week old *H2b*$^{fl/fl}$ and *H2b*$^{\Delta IEC}$ mice.

(D) MODE-K WT and STING$^{-/-}$ cells were transfected with either siRNA against *Rnaseh2b* or control siRNA for 24h. Protein levels were measured by western blot assay.

(E) Schematic of generation of *H2b*$^{\Delta IEC}$/*STING*$^{-/-}$ mouse line.

(F) Representative picture of small intestinal tumor from aged (>53W) *H2b*$^{\Delta IEC}$/*STING*$^{-/-}$ mouse.

(G and **H)** Tumor incidence (G) and tumors per mouse (H) in *H2b*$^{fl/fl}$ (n=12), *H2b*$^{\Delta IEC}$ (n=23), *STING*$^{-/-}$ (n=18), *H2b*$^{\Delta IEC}$/*STING*$^{-/-}$ (n=37), and *H2b*/*STING*$^{\Delta IEC}$ (n=7) mice.

796 Significance was determined using unpaired two-tailed Student's test.

797 **(I)** H&E staining of *H2b*$^{\Delta IEC}$/STING$^{-/-}$ and *H2b*/*STING*$^{\Delta IEC}$ tumor

798 **(J)** Histopathological tumor grading confirms presence of adenocarcinoma of
799 *H2b*$^{\Delta IEC}$/STING$^{-/-}$ and *H2b*/*STING*$^{\Delta IEC}$ tumor.

800 **(K)** Scheme of the mouse small intestine showing regional tumor incidence based on
801 the corresponding quantification data from *H2b*$^{\Delta IEC}$/STING$^{-/-}$ mouse.

802 For all the significance analysis: ns = not significant, * $p<0.05$, ** $p<0.01$, *** $p<0.001$,
803 **** $p<0.0001$.

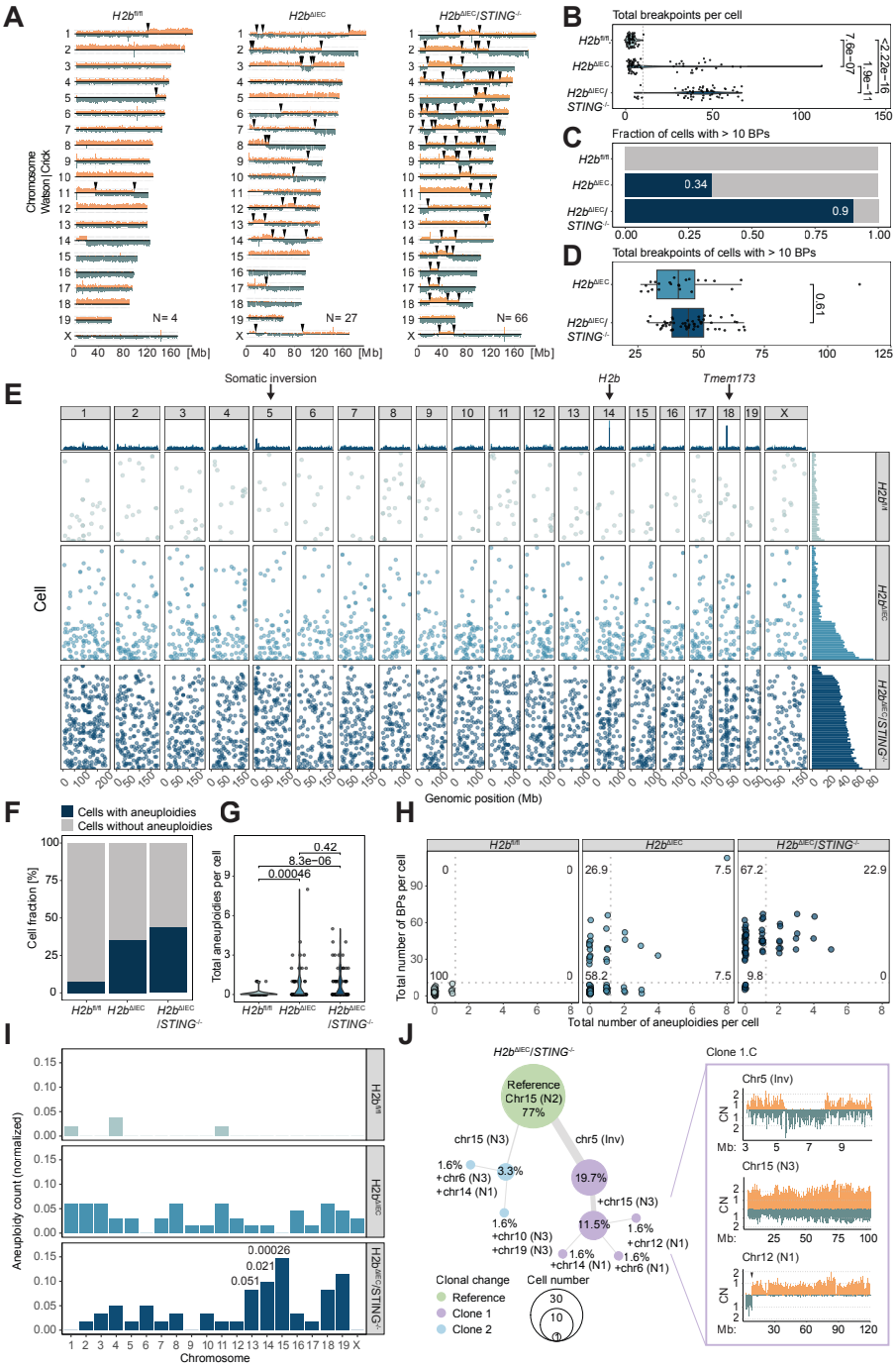

Fig. 2. Loss of STING results in chromosomal instability and clonal expansion in intestinal epithelium

(A) Representative ideograms of single cells Strand-seq libraries for *H2b*$^{fl/fl}$, *H2b*$^{\Delta IEC}$ and *H2b*$^{\Delta IEC}$/*STING*$^{-/-}$. The ideograms of each chromosome are showing binned read counts aligned to the mouse reference genome mm09. The colors indicate the positive (Crick) in blue and the negative (Watson, orange) template strand. The black arrows

811 are marking somatic changes in directionalities, or breakpoints.

812 **(B** to **D)** Quantification of breakpoints and genomic instability. (B) Violin plot showing
813 the manual quantifications of somatic breakpoints per cell by each condition. Each dot
814 represents one single cell. (C) Stack plot showing the fraction of cells with more than
815 10 BPs in blue and less or equal to 10 BPs in grey. (D) Boxplot of the total number of
816 breakpoints per cell of cells with more than 10 BPs. The P-value was calculated using
817 the two-sample t-test.

818 **(E)** The plot is showing the breakpoints per cell by genomic location, identified with
819 BreakpointR and filtered for recurrent regions identified in the *H2b*$^{fl/fl}$ cells. Each dot
820 represents a breakpoint. On the top panel the stack-histogram shows the quantification
821 per genomic position (500Kb bins). The panel on the right shows the histogram of the
822 quantification of total breakpoint per cell. Chromosome Y was removed due to the low
823 read mappability.

824 **(F)** Histogram showing the percentage of cells that possess at least one aneuploidy.

825 **(G)** Violin plot showing the number of aneuploidies per cell. Each dot represents one
826 single cell. The P-value was calculated with the two-sample t-test.

827 **(H)** Dot plot of the correlation between the count of breakpoint per cell and aneuploidy
828 per cell. The dotted grey lines mark the upper range found in *H2b*$^{fl/fl}$ cells (BPs= 10,
829 Aneuploidies= 1). The numbers shown are the percentage of cells in each quadrant.

830 **(I)** Histogram of total numbers of aneuploidies per chromosome normalized by the cell
831 number per condition. The P-value was calculated on the single-cell counts using one-
832 way analysis of variance (ANOVA) and pairwise comparisons using pairwise t-tests
833 with Benjamini-Hochberg (BH) correction for *H2b*$^{\Delta IEC}$/*STING*$^{-/-}$ vs *H2b*$^{\Delta IEC}$.

834 **(J)** Clonal expansion in *H2b*$^{\Delta IEC}$/*STING*$^{-/-}$ cells. Right panel: Network plot showing the
835 clonal fraction of cells with alterations. The black arrow is marking a somatic
836 breakpoint. Left panel: representative ideograms of regions affected in Clone 1.C.

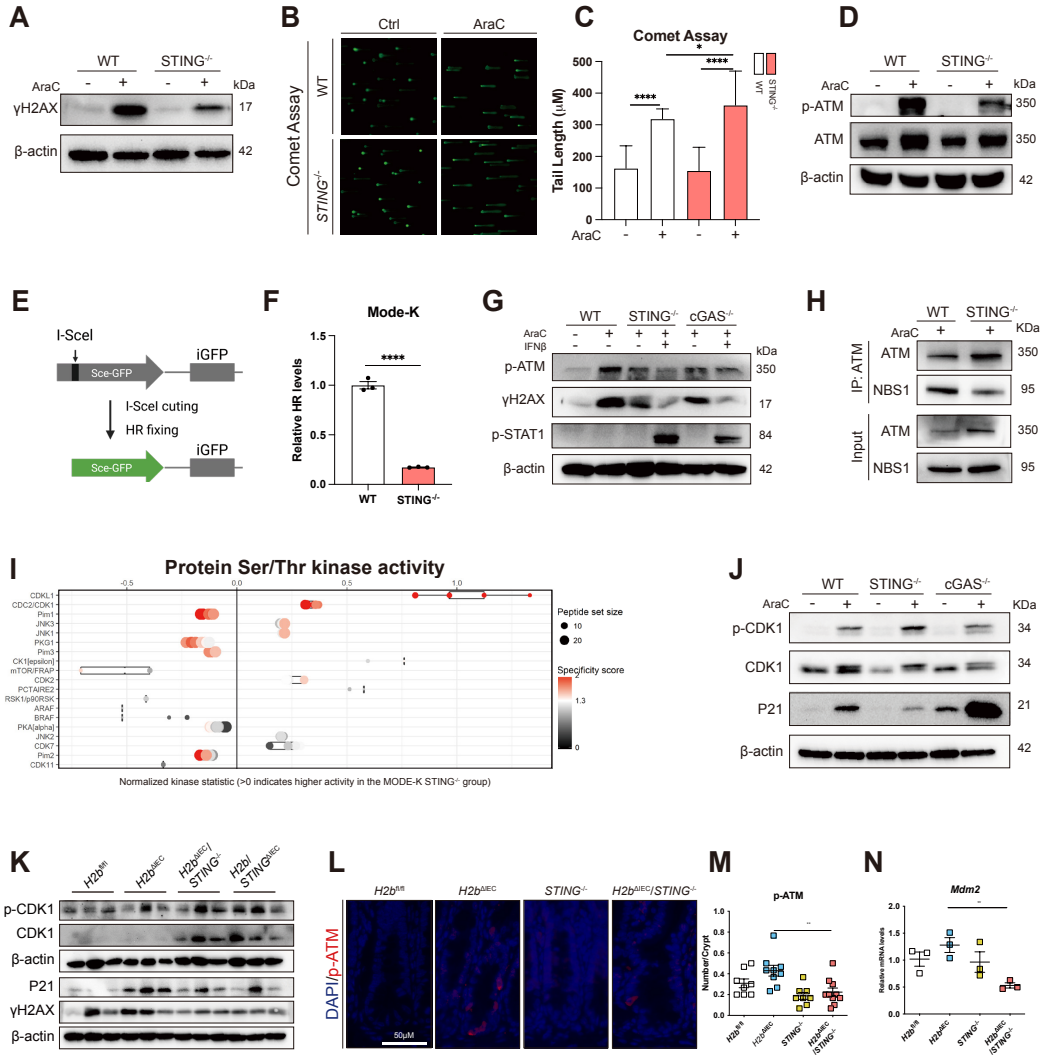

Fig. 3. STING sustains homologous recombination and G2/M checkpoint control independent of IFN-I

(A) Western blot analysis of γH2AX from MODE-K WT and STING$^{-/-}$ cell lines after treated with 2.5 μM AraC for 20h.

(B and **C)** Representative picture (B) and statistical analysis of tail length (C) measured from comet assay from MODE-K WT and STING$^{-/-}$ cell lines after treated with 2.5 μM AraC for 20h. Significance was determined using unpaired two-tailed Student's test.

(D) Western blot analysis of ATM from MODE-K WT and STING$^{-/-}$ cell lines after treated with 2.5 μM AraC for 20h.

(E and **F)** Scheme of DR-GFP reporter assay (E). HR levels of MODE-K WT and STING$^{-/-}$ cell lines were measured by FACS (F). Significance was determined using

849 unpaired two-tailed Student's test.

850 **(G)** MODE-K WT and STING$^{-/-}$ cells were transfected with either siRNA against *Wip1*
851 or control siRNA for 24h then stimulated with 2.5 μM AraC for 20h. Protein levels
852 were measured by western blot assay.

853 **(H)** Co-immunoprecipitation (co-IP) analysis of the interaction between ATM and
854 NBS1 from MODE-K WT and STING-/- cell lines after treated with 2.5 μM AraC for
855 20h. ATM-containing complexes were immunoprecipitated using an anti-ATM
856 antibody and probed for NBS1 by immunoblotting.

857 **(I)** Deeper look into the results from upstream kinase analysis showing the main
858 affected STK, the full figure shown in **fig. S9D**.

859 **(J)** MODE-K WT, STING$^{-/-}$, and cGAS$^{-/-}$ cells were treated with 2.5 μM AraC for 20h.
860 Protein levels were analyzed by western blot.

861 **(K)** Protein levels from young (8-12W) *H2b*$^{fl/fl}$, *H2b*$^{\Delta IEC}$, *H2b*$^{\Delta IEC}$/*STING*$^{-/-}$,
862 *H2b*/*STING*$^{\Delta IEC}$ mouse small intestine crypt sample assessed by western blot assay.

863 **(L** and **M)** Immunohistochemistry and statistical analysis of the small intestine of aged
864 (>53W) H2bfl/fl (n=8), *H2b*$^{\Delta IEC}$ (n=9), STING$^{-/-}$ (n=8) and *H2b*$^{\Delta IEC}$/*STING*$^{-/-}$ (n=10)
865 mice, stained for p-ATM. Representative images (L) of p-ATM immunofluorescence
866 staining (red) and corresponding statistics (M). The average number of p-ATM-positive
867 cells per crypt was determined by counting ≥30 crypts per sample, and the mean number
868 of positive cells per crypt was calculated. Significance was determined using unpaired
869 two-tailed Student's test.

870 **(N)** Gene expression of *Mdm2* in *H2b*$^{fl/fl}$, *H2b*$^{\Delta IEC}$, *STING*$^{-/-}$ and *H2b*$^{\Delta IEC}$/*STING*$^{-/-}$ mice
871 assessed by qPCR taqman probe assay, n=3. Significance was determined using
872 unpaired two-tailed Student's test.

873 For all the significance analysis: ns = not significant, * $p<0.05$, ** $p<0.01$, *** $p<0.001$,
874 **** $p<0.0001$.

875

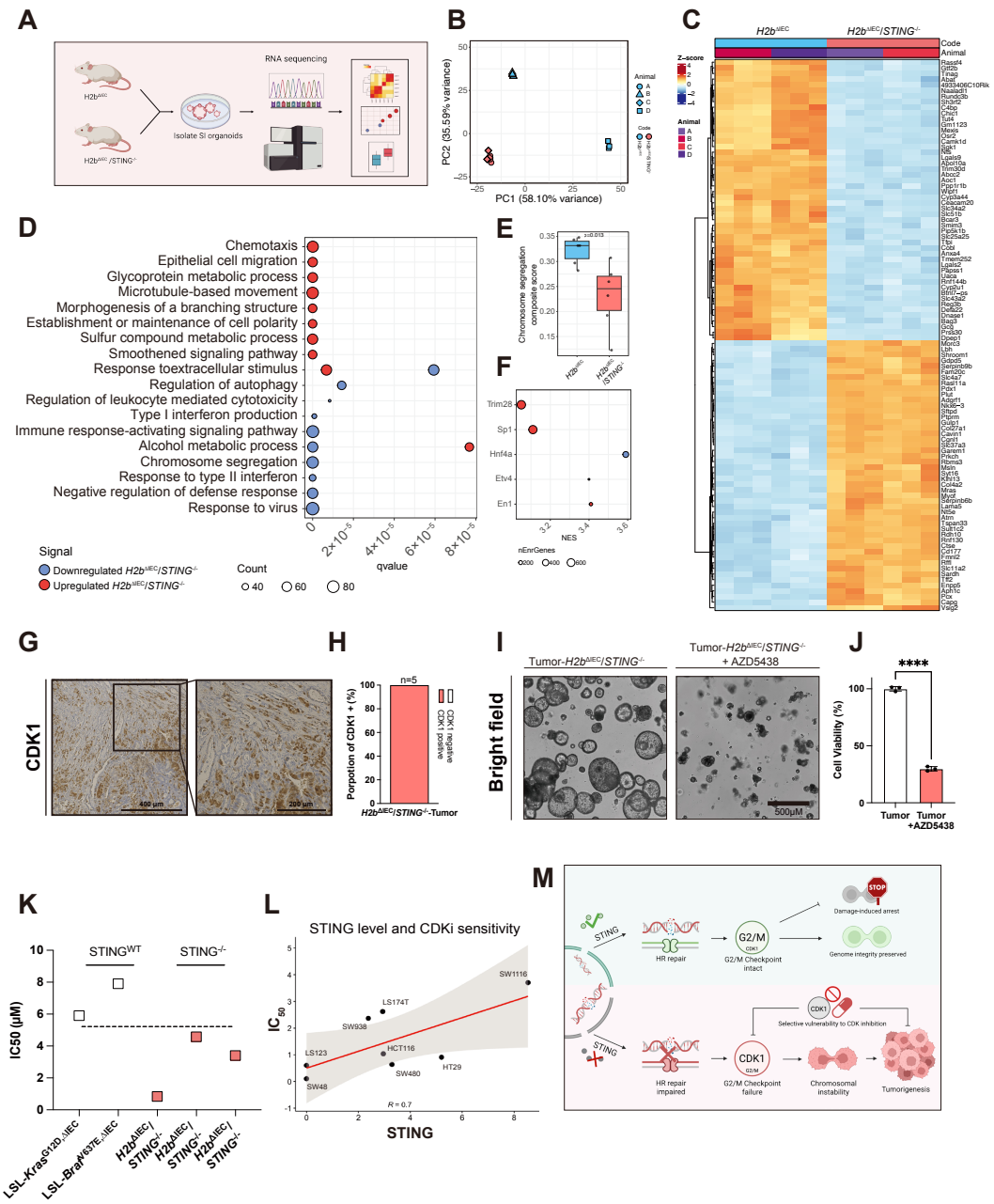

Fig. 4. STING loss rewires DNA damage–associated transcriptional programs and confers vulnerability to CDK inhibition

(A to **F)** RNA-seq identifies distinct transcriptional programs in *H2b*$^{\Delta IEC}$ and *H2b*$^{\Delta IEC}$/*STING*$^{-/-}$ Organoids. Scheme of RNA-seq model (A). Principal component analysis (PCA) of RNAseq samples. *H2b*$^{\Delta IEC}$/*STING*$^{-/-}$ samples clustered tightly and were independent of the animal of origin, whereas *H2b*$^{\Delta IEC}$ samples segregated from *H2b*$^{\Delta IEC}$/*STING*$^{-/-}$ along both principal components and also separated by animal of

884 origin along PC2 (B). Heatmap of the top 50 differentially expressed genes (DEGs)
885 between *H2b*$^{\Delta IEC}$ and *H2b*$^{\Delta IEC}$/*STING*$^{-/-}$ group. DEG expression profiles were highly
886 concordant between animals within each genotype, with robust differences between
887 genotypes; in *H2b*$^{\Delta IEC}$/*STING*$^{-/-}$ group, 2,388 genes were upregulated and 2,612 genes
888 were downregulated relative to *H2b*$^{\Delta IEC}$ (C). Gene Ontology (GO) overrepresentation
889 analysis for DEGs upregulated (red) and downregulated (blue) in *H2b*$^{\Delta IEC}$/*STING*$^{-/-}$
890 group. Dot size indicates the number of genes associated with each enriched term. The
891 top 10 GO terms per direction were selected based on term dispensability calculated
892 using rrvgo (D). Transcription factor binding site (TFBS) enrichment analysis for DEGs
893 upregulated (red) and downregulated (blue) in *H2b*$^{\Delta IEC}$/*STING*$^{-/-}$ group. Dot size
894 indicates the number of genes associated with each enriched transcription factor (E).
895 Single-sample GSEA (ssGSEA) score for nuclear chromosome segregation. Based on
896 the RNA-seq data described above, ssGSEA was performed to calculate pathway
897 activity scores for nuclear chromosome segregation using the MSigDB gene set
898 GOBP_NUCLEAR_CHROMOSOME_SEGREGATION (F).
899 **(G** and **H)** Immunohistochemical staining of CDK1 in tumor tissues derived from
900 H2b$^{\Delta IEC}$/STING$^{-/-}$ mice. Representative picture of CDK1 staining(G). Proportion of
901 CDK1-positive tumors (H).
902 **(I** and **J)** Representative pictures (I) and CellTiter-Glo assay (J) from *H2b*$^{\Delta IEC}$/*STING*$^{-}$
903 $^{/-}$ tumor organoids treated with Control (DMSO) or 1 μM AZD5438 for 72h.
904 Significance was determined using unpaired two-tailed Student's test.
905 **(K)** Comparison of AZD5438 IC_{50} values in STING^{WT} and STING$^{-/-}$ tumor organoids.
906 IC_{50} values for AZD5438 were determined from dose–response assays and compared
907 between STING^{WT} tumor organoids and STING$^{-/-}$ tumor organoids based on the dose-
908 response curve shown in **fig. S12B** to **F**.
909 **(L)** Correlation between AZD5438 sensitivity and STING expression in CRC cell lines.
910 Linear regression analysis was performed to assess the relationship between AZD5438
911 sensitivity (IC_{50} values in different colorectal cancer cell lines; **fig. S12G** to **N**) and
912 STING protein levels determined by western blot (**fig. S12O**; quantified by
913 densitometry as indicated).
914 **(M)** Proposed model for epithelial STING function in genome integrity control. In
915 epithelial cells, STING supports HR repair and maintains G2/M checkpoint integrity,
916 thereby enabling damage-**induced** arrest and preserving genome stability. Loss of

917 STING impairs HR repair, weakens G2/M checkpoint control in association with
918 increased CDK1 activity, and promotes chromosomal instability, ultimately
919 contributing to tumorigenesis. This checkpoint-defective state is accompanied by
920 selective vulnerability to CDK inhibition.
921 For all the significance analysis: ns = not significant, * p<0.05, ** p<0.01, *** p<0.001,
922 **** p<0.0001.
923

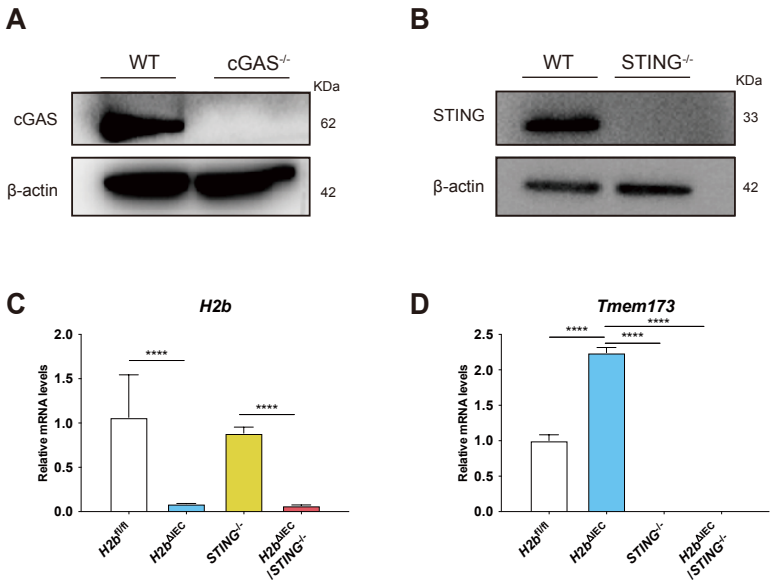

924
925 **Fig. S1. Genotype validation of knockout cell lines and mouse lines**
926 **(A** to **B)** Western blot validation of MODE-K cGAS$^{-/-}$ (A) and STING$^{-/-}$ (B) knock out cell
927 lines.
928 **(C** to **D)** Genotyping of mouse lines using primers/probes targeting *H2b* (C) and
929 *Tmem173* (D) in *H2b*$^{fl/fl}$, *H2b*$^{\Delta IEC}$,*STING*$^{-/-}$ and *H2b*$^{\Delta IEC}$/*STING*$^{-/-}$ mice. *H2b* and
930 *Tmem173* transcript levels across the four genotypes were quantified in parallel, as
931 indicated. Significance was determined using unpaired two-tailed Student's test.
932 For all the significance analysis: ns = not significant, * p<0.05, ** p<0.01, *** p<0.001,
933 **** p<0.0001.
934

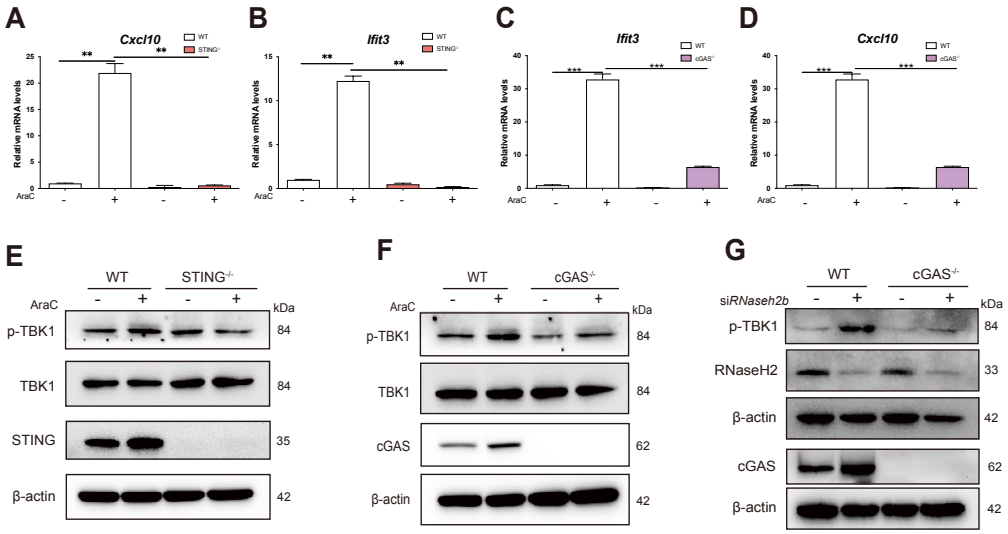

Fig. S2. cGAS–STING-dependent IFN-I responses to DNA damage

(A and **D)** Gene expression of IFN-I pathway genes *Cxcl10* and *Ifit3* quantified by Taqman assay from MODE-K STING$^{-/-}$ (A-B) or cGAS$^{-/-}$ (C-D) cells were treated with 2.5 μM AraC for 20h, relative to MODE-K WT. Significance was determined using unpaired two-tailed Student's test.

(E) MODE-K WT and STING$^{-/-}$ cells were treated with 2.5 μM AraC for 20h. Protein levels were measured by western blot assay.

(F) MODE-K WT and cGAS$^{-/-}$ cells were treated with 2.5 μM AraC for 20h. Protein levels were measured by western blot assay.

(G) MODE-K WT and cGAS$^{-/-}$ cells were transfected with either siRNA against *Rnaseh2b* or control siRNA for 24h. Protein levels were measured by western blot assay.

For all the significance analysis: ns = not significant, * $p<0.05$, ** $p<0.01$, *** $p<0.001$, **** $p<0.0001$.

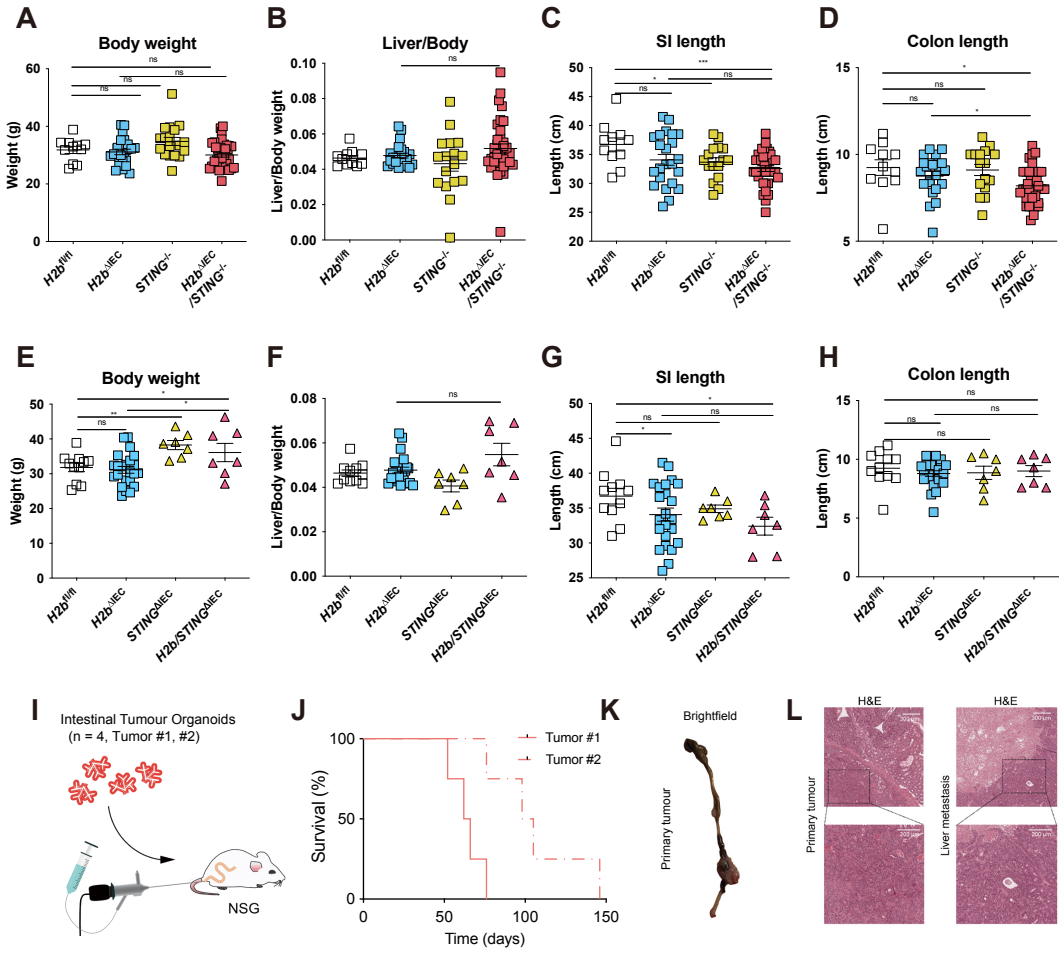

951

952 **Fig. S3. Clinical phenotype in aged *H2b*$^{\Delta IEC}$/*STING*$^{-/-}$ mice**

953 **(A** to **D)** Basal phenotyping analysis including Body weight (A), liver weight/body
954 weight (B), Small intestine length (C), Colon length of aged (D) (> 53W) *H2b*$^{fl/fl}$ (n=12),
955 *H2b*$^{\Delta IEC}$ (n=23) ,*STING*$^{-/-}$ (n=18) and *H2b*$^{\Delta IEC}$/*STING*$^{-/-}$ (n=37) mouse line. Significance
956 was determined using unpaired two-tailed Student's test.

957 **(E** to **H)** Clinical phenotype in aged *H2b*/*STING*$^{\Delta IEC}$ mice. Basal phenotyping analysis
958 including body weight (E), liver weight/body weight (F), small intestine length (G), colon
959 length (H) of aged (> 53W) *H2b*$^{fl/fl}$ (n=12), *H2b*$^{\Delta IEC}$ (n=23) ,*STING*$^{\Delta IEC}$ (n=7) and
960 *H2b*/*STING*$^{\Delta IEC}$ (n=7). *H2b*$^{fl/fl}$ and *H2b*$^{\Delta IEC}$ mice are shared controls from the same
961 cohort as shown in fig. S3 A-D. Significance was determined using unpaired two-tailed
962 Student's test.

963 **(I)** Scheme of tumor organoid transplant model.

964 **(J** to **L)** Survival curve of mice transplanted with tumor organoids isolated from

965 *H2b*$^{\Delta IEC}$/*STING*$^{-/-}$ mouse (J). Representative picture of primary tumor (K). H&E staining
966 of primary and metastatic tumor (L).
967 For the significance analysis: ns = not significant, * $p<0.05$, ** $p<0.01$, *** $p<0.001$, ****
968 $p<0.0001$.

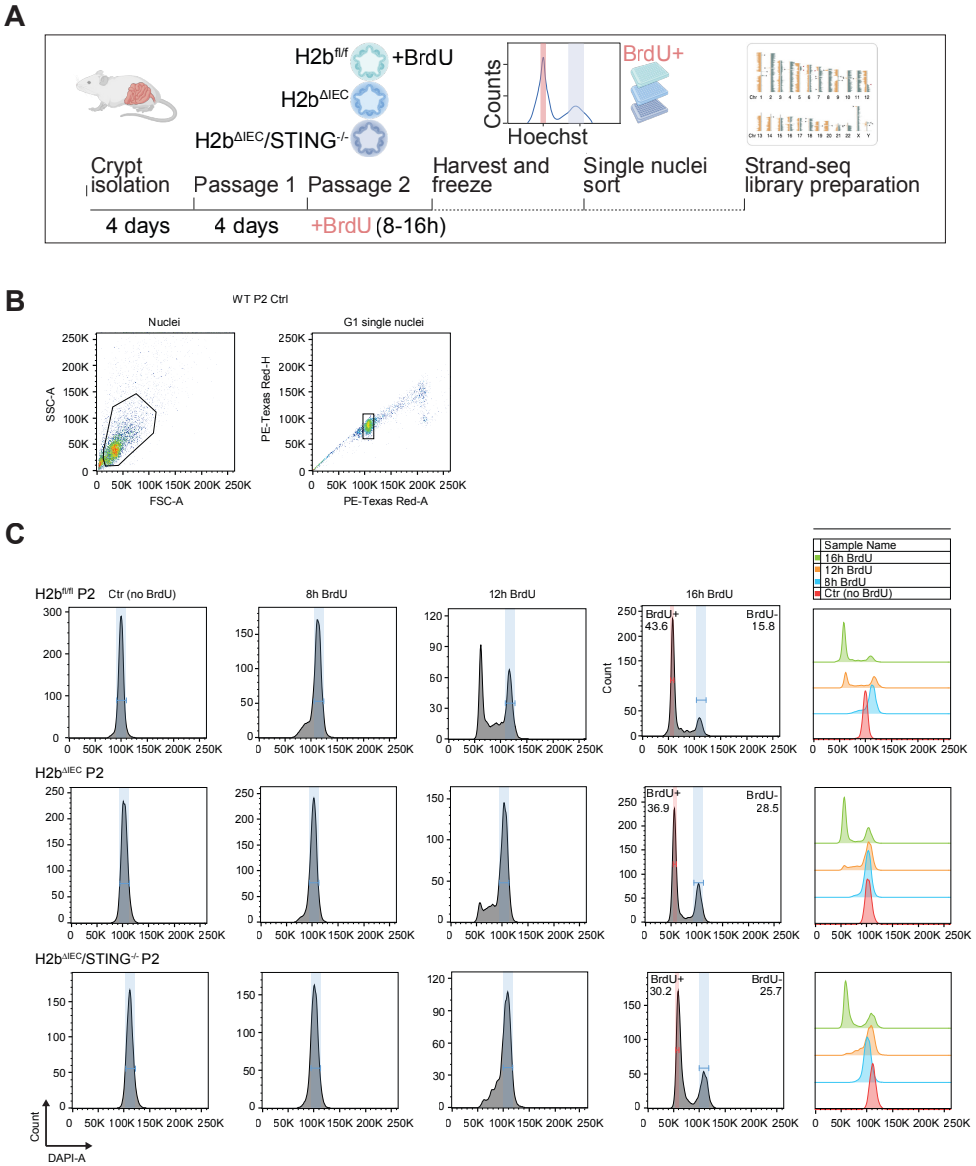

Fig. S4. Experimental setup to produce Strand-seq libraries and FACS gating strategy

(A) Graphical design of experimental setup to produce Strand-seq libraries.

(B) Example of the FACS gating used to select intact nuclei in G1 phase.

(C) FACS gates showing the histogram counts of the DAPI-A channel for cells untreated with BrdU (Ctr), treated for 8, 12 or 16 hours with BrdU. The gate in blue shows the undivided peak (BrdU-), while the red gate indicates the nuclei of cells that divided once in presence of BrdU (hemi-substituted, BrdU+).

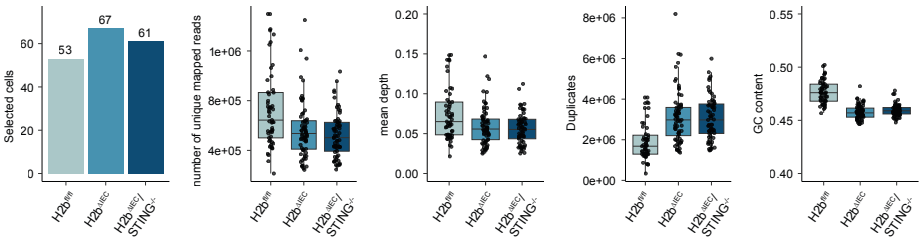

979

980 **Fig. S5. Strand-seq libraries quality**

981 Histogram showing the number of selected cells per sample. The boxplots are showing
982 the quality control of the selected libraries. Specifically showing the number of unique
983 mapped reads, mean depth, duplicates and GC content. Each dot represents one
984 single cell.

985

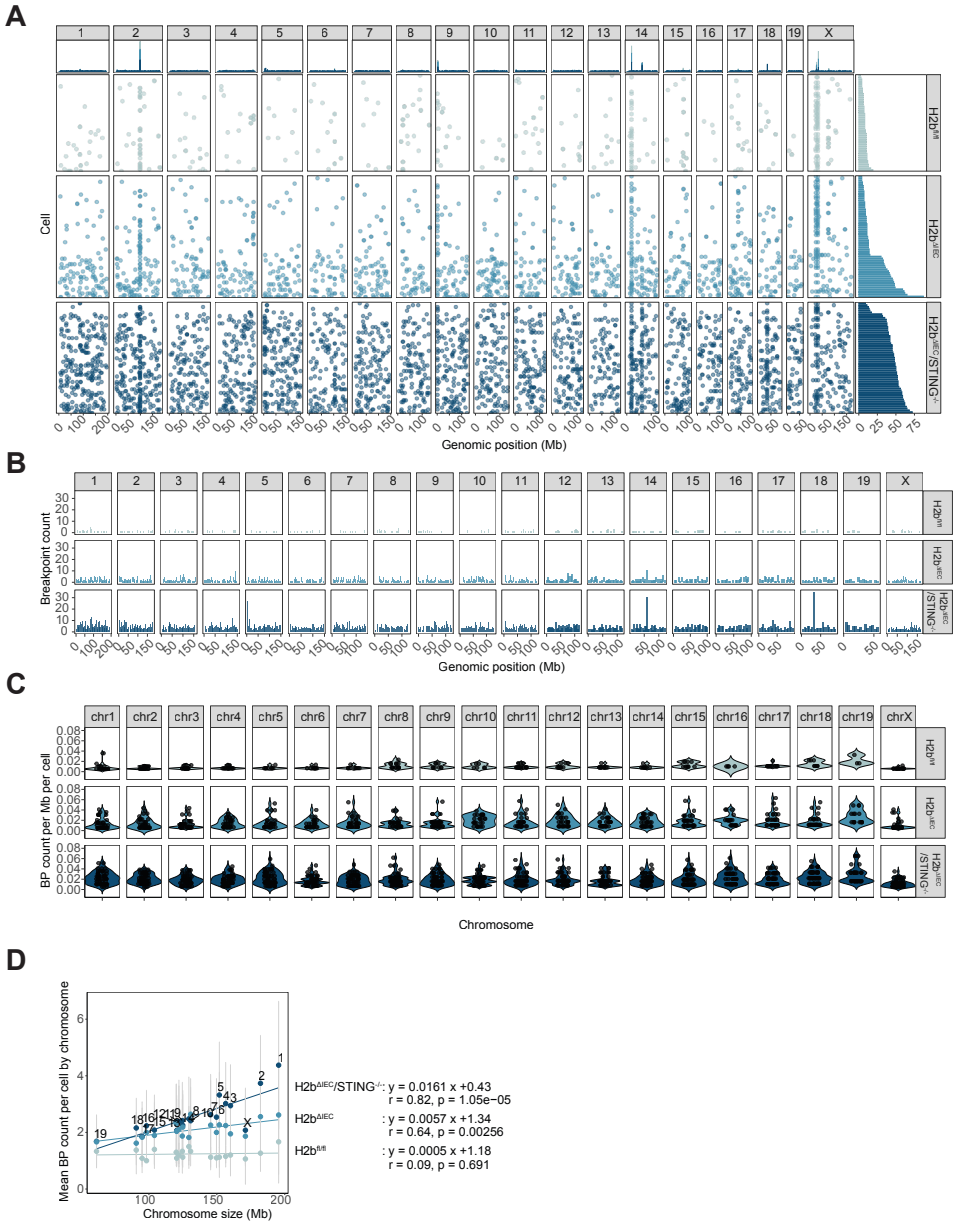

Fig. S6. Breakpoint analysis and filtering strategy

(A) The plot is showing the breakpoints per cell by genomic location, identified with BreakpointR. Each dot represents a breakpoint. On the top panel the stack-histogram shows the quantification per genomic position (500 Kb bins). The panel on the right shows the histogram of the quantification of total breakpoint per cell. Chromosome Y was removed due to the low read mappability.

(B) Histogram histogram shows the quantification of breakpoints per genomic position

994 (4Mb binned genome) after filtering for *H2b*$^{fl/fl}$ (WT) specific-recurrent regions.

995 **(C)** Violin plot of the BP count per Mb by chromosome.

996 **(D)** The plot shows the correlation between the chromosome size and the median BP

997 count per chromosome. The grey bar represents the standard deviation for each

998 chromosome and condition.

999

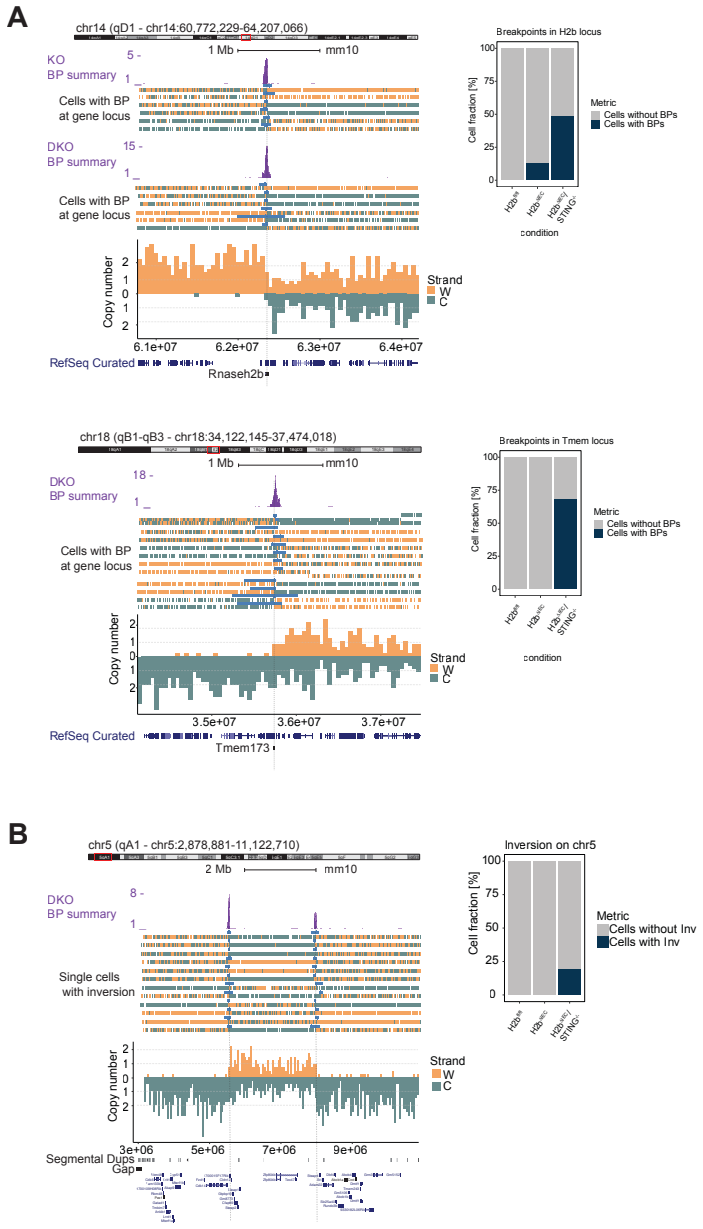

Fig. S7. Breakpoint enrichment at specific loci

(A) UCSC visualization of the accumulation of breakpoints at *H2b* (left-upper panel) and *Sting* loci (left-lower panel). The violet histogram represents the overlapping BP count. The blue bar is the confidence interval of the BP per cell. Each row is a single cell, and the directionality can be visualized by the vertical bars that are binned reads (Watson= orange; Crick= green). At the bottom a mirrored plot of a representative cell

1008 possessing a BP at the gene locus. Right panels: Percentage of cell fraction with
1009 breakpoints on the H2b and Sting loci.
1010 **(B**) Representative ideograms of inverted region and UCSC visualization of the
1011 accumulation of breakpoints at the inversion borders. The violet histogram represents
1012 the overlapping BP count. The blue bar is the confidence interval of the BP per cell.
1013 Each row is a single cell, and the directionality can be visualized by the vertical bars
1014 that are binned reads (Watson= orange; Crick= green). Right panels: Percentage of
1015 cell fraction with inversion.
1016

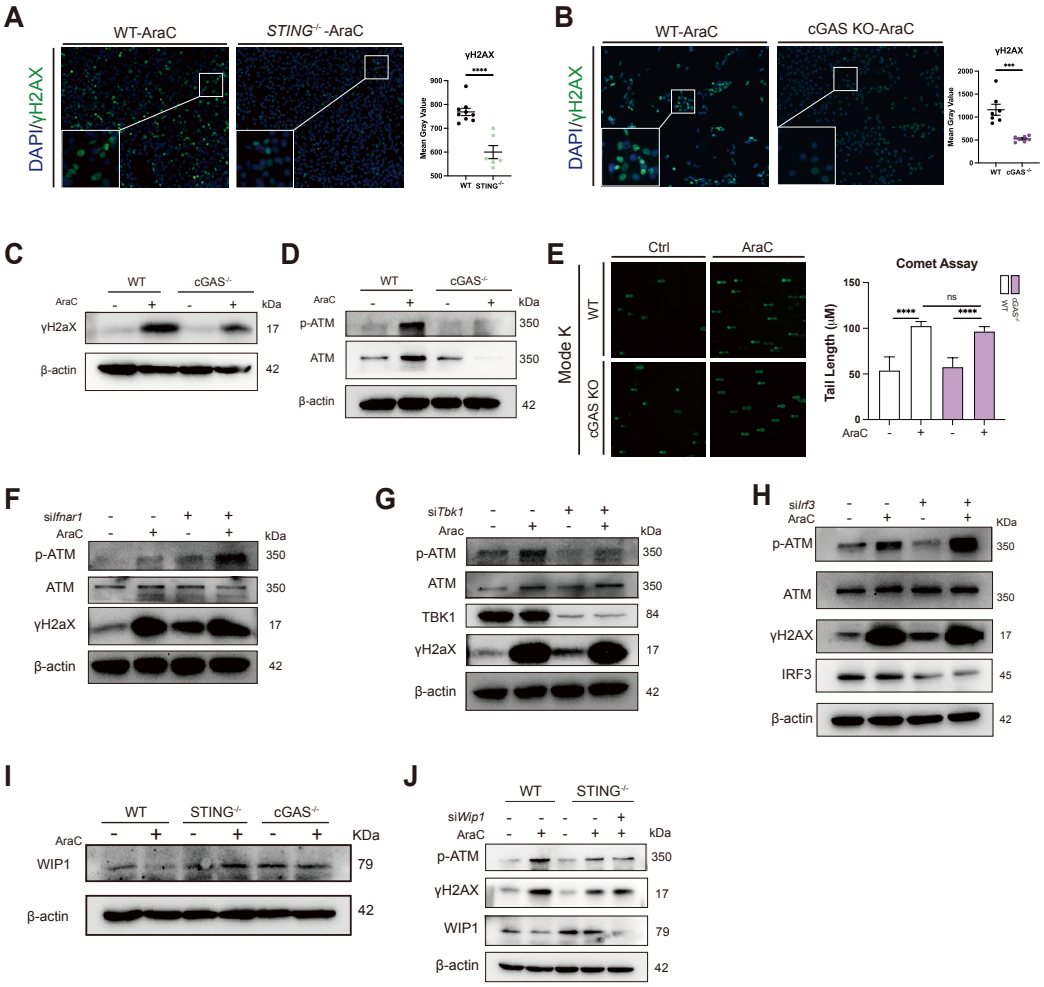

Fig. S8. cGAS-STING pathway regulates HR in an IFN-I independent manner

(A-B) Immunofluorescence staining of γH2AX following AraC treatment in MODE-K cells. MODE-K STING$^{-/-}$ (A) and MODE-K cGAS$^{-/-}$ (B) cells were treated with 2.5 μM AraC for 20 h and stained for γH2AX by immunofluorescence. Representative images (Left) and quantification of nuclear γH2AX fluorescence intensity (Right) are shown for each genotype. Each dot represents the mean nuclear γH2AX fluorescence intensity across all cells within a single image. Significance was determined using unpaired two-tailed Student's test.

(C-D) HR related protein γH2AX (C) and ATM (D) assessed by western blot in MODE-K cGAS$^{-/-}$ cells.

(E) MODE-K cGAS$^{-/-}$ cells were treated with 2.5 μM AraC for 20 h and subjected to a comet assay. DNA damage level was quantified by measuring comet tail length. Significance was determined using unpaired two-tailed Student's test.

1031 **(F**) MODE-K WT, STING$^{-/-}$, and cGAS$^{-/-}$ cells were treated with 2.5 μM AraC and/or
1032 100ng/ml IFN-β for 20 h, as indicated. Protein levels were analyzed by western blot.
1033 **(G** to **I**) **siRNA-mediated knockdown of canonical cGAS/STING pathway. MODE-**
1034 **K WT** cell was transfected with siRNAs targeting *Ifnar**1***(**G**), ***Tbk1***(**H**), ***Irf3*** (**I**) or with a
1035 non-targeting control siRNA, then stimulated with 2.5 μM AraC for 20h. Protein levels
1036 were measured by western blot assay.
1037 **(J)** MODE-K WT, STING$^{-/-}$, and cGAS$^{-/-}$ cells were treated with 2.5 μM AraC for 20h.
1038 Protein levels were analyzed by western blot.
1039 For all the significance analysis: ns = not significant, * $p<0.05$, ** $p<0.01$, *** $p<0.001$,
1040 **** $p<0.0001$.
1041

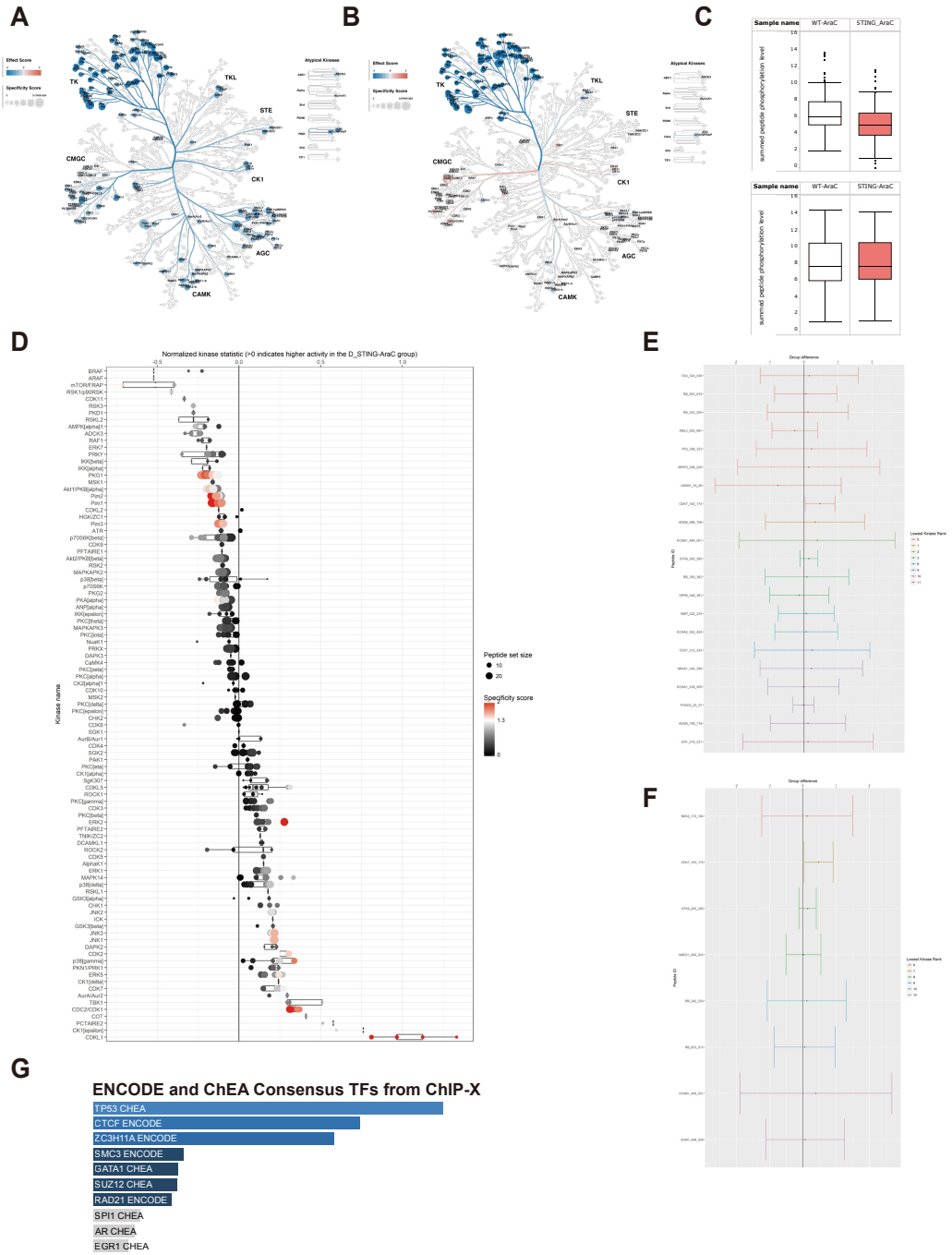

Fig. S9. Phospho-kinase profiling reveals altered kinase activity networks in MODE-K STING$^{-/-}$ cells under control and AraC treatment

(A and **B)** Kinome tree visualization of upstream kinase activity in MODE-K cells. Upstream kinase analysis results are mapped onto the kinome tree, comparing MODE-K STING$^{-/-}$ with WT under control (A) conditions and AraC (B) treatment. Colors indicate relative kinase activity in MODE-K STING$^{-/-}$ versus WT (blue, decreased; red,

1050 increased).

1051 **(C)** Box plots showing the sum of log2-transformed fluorescence signal intensities of
1052 tyrosine kinase (PTK) phosphorylation levels on the chip.

1053 **(D)** Upstream kinase analysis based on degree of phosphorylation from serine-
1054 threonine kinase assay (STK) of MODE-K STING$^{-/-}$ compared with WT. Based on
1055 activity and phosphorylation pattern a prediction of the active kinase is given by the
1056 BioNavigator 6 software. Size of the peptide set is shown by dot size. Color code
1057 ranges from red (high specificity) to black (low specificity) and kinases are sorted by
1058 specificity score.

1059 **(E** and **F)** Representative peptides supporting kinase assignment. Representative
1060 peptide signals are shown for (E) CDK1 and (F) CDKL1.

1061 **(G)** EnrichR pathway enrichment based on upstream kinase analysis. Kinases inferred
1062 to have decreased or increased activity in AraC treated MODE-K STING$^{-/-}$ compared
1063 with WT were converted to gene names and used as input for EnrichR. Bar plots show
1064 enriched terms ranked by significance (logP; top to bottom), with decreased-activity
1065 kinases shown in the upper panel and increased-activity kinases shown in the lower
1066 panel.

1067

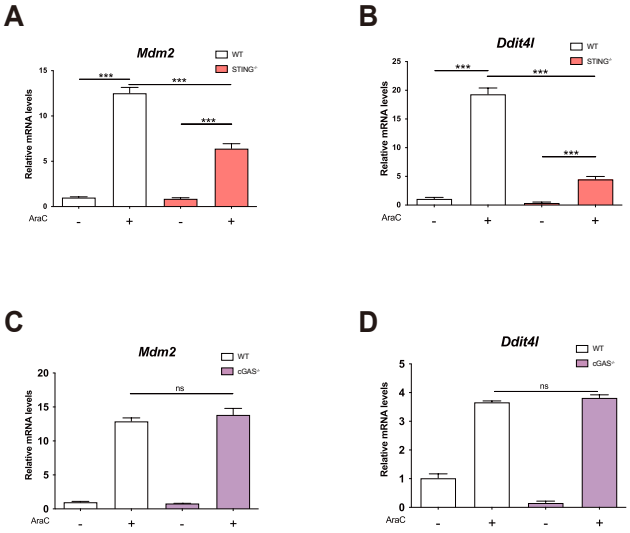

Fig. S10. Differential roles of STING and cGAS in regulating DNA damage-induced p53 signaling via *Ddit4l*

(A and **B)** Gene expression of *Mdm2* and *Ddit4l* quantified by Taqman assay from MODE-K STING$^{-/-}$ cells treated with 2.5 μM AraC for 24h, relative to MODE-K WT. Significance was determined using unpaired two-tailed Student's test.

(C and **D)** Gene expression of *Mdm2* and *Ddit4l* quantified by Taqman assay from MODE-K cGAS$^{-/-}$ cells treated with 2.5 μM AraC for 24h, relative to MODE-K WT. Significance was determined using unpaired two-tailed Student's test.

For all the significance analysis: ns = not significant, * $p<0.05$, ** $p<0.01$, *** $p<0.001$, **** $p<0.0001$.

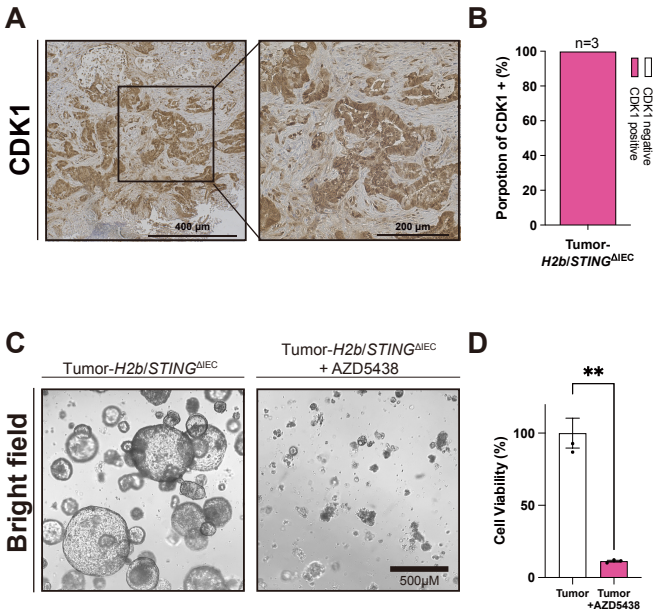

1080

1081 **Fig. S11. STING-deficient tumors exhibit elevated CDK1 activity and vulnerability**
1082 **to CDK inhibition**

1083 **(A** and **B)** Immunohistochemical staining of CDK1 in tumor tissues derived from
1084 H2b/STING$^{\Delta IEC}$ mice. Representative picture of CDK1 staining (A). Proportion of
1085 CDK1-positive tumors (B).

1086 **(C** and **D)** Representative pictures (C) and CellTiter-Glo assay (D) from *H2b*/*STING*
1087 $^{\Delta IEC}$ tumor organoids treated with Control (DMSO) or 1 µM AZD5438 for 72h.
1088 Significance was determined using unpaired two-tailed Student's test.

1089 For all the significance analysis: ns = not significant, * $p<0.05$, ** $p<0.01$, *** $p<0.001$,
1090 **** $p<0.0001$.

1091

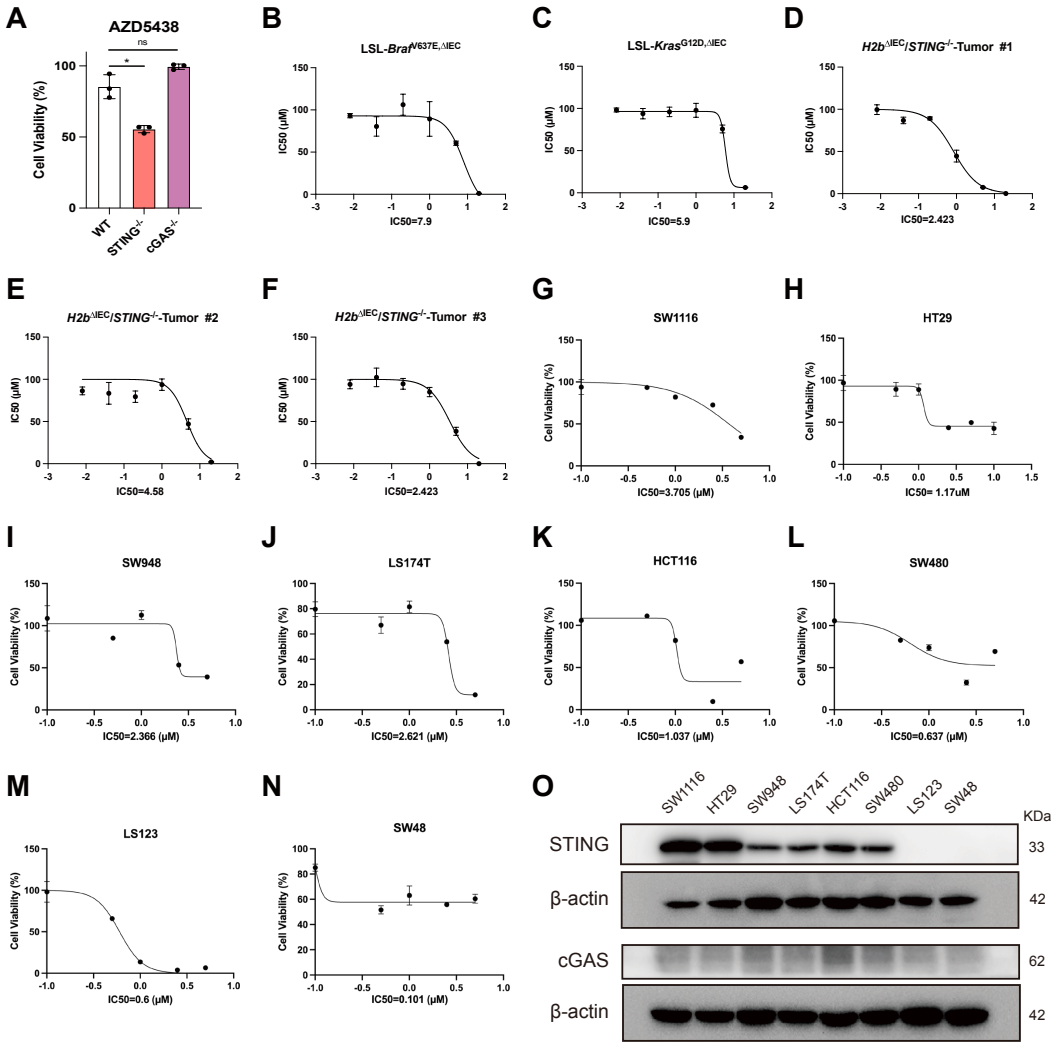

Fig. S12. STING axis status associates with CDK inhibitor response in mouse tumor organoids and human CRC cell lines

(A) Cell viability following AZD5438 treatment in MODE-K cell lines. MODE-K WT, STING-/-, and cGAS-/- cells were treated with 1 μM AZD5438 for 72 h. Cell viability was assessed using the CellTiter-Glo luminescent cell viability assay. Significance was determined using unpaired two-tailed Student's test.

(B to **F)** AZD5438 dose–response and IC50 determination in tumor organoids. Tumor organoids were treated with a gradient of AZD5438 (Ctrl, 0.25, 0.5, 1, 2.5, and 5 μM) for 3 days. Cell viability was quantified using the CellTiter-Glo luminescent assay, and dose–response curves were used to calculate IC_{50} values. IC_{50} values in SI tumor organoids derived from LSL-Braf$^{V637E,\Delta IEC}$ mouse line (B). IC_{50} in LSL-Kras$^{G12D,\Delta IEC}$

1104 tumor organoids (C). IC_{50} values in different *H2b*/*STING*$^{\Delta IEC}$ mouse (D-F).

1105 **(G** to **N)** AZD5438 dose–response and IC50 determination in human colon
1106 adenocarcinoma cell lines. Indicated human colon adenocarcinoma cell lines were
1107 treated with a gradient of AZD5438 (Ctrl, 0.25, 0.5, 1, 2.5, and 5 μM) for 3 days. Cell
1108 viability was quantified using the CellTiter-Glo luminescent assay, and dose–response
1109 curves were generated to calculate IC_{50} values for each cell line.

1110 **(O**) cGAS-STING protein levels in human colon adenocarcinoma cell lines were
1111 assessed by western blot.

1112 For all the significance analysis: ns = not significant, * $p<0.05$, ** $p<0.01$, *** $p<0.001$,
1113 **** $p<0.0001$.

1114

1115

1116 **Table S1: Antibody List**

Antibody	Source	Catalog	Dillution	Usage
STING	Cell Signaling Technology	13647S	1:1000	WB
ATM	Cell Signaling Technology	2873T	1:1000	WB
p-ATM	santacruz	sc-47739	1:1000	WB
cGAS	Cell Signaling Technology	31659S	1:1000	WB
P53	Cell Signaling Technology	2524S	1:1000	WB
TBK1	Cell Signaling Technology	3013S	1:1000	WB
p-TBK1	Cell Signaling Technology	5483S	1:1000	WB
γH2AX	Cell Signaling Technology	2577S	1:1000	WB
WIP1	Cell Signaling Technology	11901	1:1000	WB
cdc2 (CDK1)	Cell Signaling Technology	28439S	1:1000	WB
p-cdc2(p-CDK1 T161)	Cell Signaling Technology	9114S	1:1000	WB
P21	Cell Signaling Technology	37543S	1:1000	WB
RnaseH2	Shared by collaborator (*2*)	-	1:1000	WB
NBS1	Cell Signaling Technology	14956	1:1000	WB
β-actin	Cell Signaling Technology	4970S	1:3000	WB
IRF3	abcam	ab76493	1:1000	WB
mouse HRP	Amersham Biosciences	NA931V	1:2000	WB
rabbit HRP	Amersham Biosciences	NA934V	1:2000	WB
p-ATM	santacruz	sc-47739	1:100	IF
γH2AX	Cell Signaling Technology	2577S	1:500	IF
Alexa Fluor 488-goat anti-rabbit	Thermo Fisher Scientific	A11070	1:500	IF
cdc2 (CDK1)	Cell Signaling Technology	28439S	1:500	IHC
rabbit HRP	Amersham Biosciences	NA934V	1:2000	IHC
NBS1	Cell Signaling Technology	14956	1:100	co-IP
ATM	abcam	ab201022	1:100	co-IP

1117

1118

1119 **Table S2. Primer list**

Gene name	Source	Ref ID
Rnaseh2b	IDT	Mm.PT.56a.41665482
β-actin (*Actb*)	IDT	Mm.PT.39a.22214843.g
Tmem173	IDT	Mm.PT.58.12798185
Mdm2	IDT	Mm.PT.58.42166864
Ddit4l	IDT	Mm.PT.58.32152752
Cxcl10	IDT	Mm.PT.58.43575827
Ifit3	IDT	Mm.PT.58.33537107

1120

1121

1122 **Table S3. siRNA list**

Gene name	Source	Catalog
Rnaseh2b	QIAGEN	GS67153
Ddit4l	QIAGEN	GS73284
Tmem173	QIAGEN	GS72512
cgas	QIAGEN	GS214763
Wip1	Thermofisher	s79351
Ifnal1	QIAGEN	GS15975
Irf3	QIAGEN	GS54131
Trp53	QIAGEN	GS22059

1123

1124

1125 **Table S4. stimulants list**

Name	Source	Catalog
AraC	Sigma-Aldrich	C6645-25mg
AZD5438	MCE	HY-10012
AZD0156	MCE	HY-100016
rm IFN-beta Protein (with carrier)	R&D Systems	8234-MB-010

1126

1127

1128 **References and Notes:**

1129 1. V. Bonis, C. Rossell, H. Gehart, The Intestinal Epithelium - Fluid Fate and Rigid Structure From
1130 Crypt Bottom to Villus Tip. *Front Cell Dev Biol* **9**, 661931 (2021).
1131 2. M. A. M. Reijns *et al.*, Enzymatic removal of ribonucleotides from DNA is essential for
1132 mammalian genome integrity and development. *Cell* **149**, 1008-1022 (2012).
1133 3. K. Aden *et al.*, Epithelial RNase H2 Maintains Genome Integrity and Prevents Intestinal
1134 Tumorigenesis in Mice. *Gastroenterology* **156**, 145-159 e119 (2019).
1135 4. L. Welz *et al.*, Epithelial X-Box Binding Protein 1 Coordinates Tumor Protein p53-Driven DNA
1136 Damage Responses and Suppression of Intestinal Carcinogenesis. *Gastroenterology* **162**, 223-
1137 237.e211 (2022).
1138 5. N. Kakavand *et al.*, Atg16l1 and Xbp1 cooperatively protect from transcription-associated
1139 mutagenesis and small intestinal carcinogenesis. *Oncogene*, (2025).
1140 6. A. Sassa, M. Yasui, M. Honma, Current perspectives on mechanisms of ribonucleotide
1141 incorporation and processing in mammalian DNA. *Genes and Environment* **41**, 3 (2019).
1142 7. M. Motwani, S. Pesiridis, K. A. Fitzgerald, DNA sensing by the cGAS-STING pathway in
1143 health and disease. *Nat Rev Genet* **20**, 657-674 (2019).
1144 8. H. Liu *et al.*, Nuclear cGAS suppresses DNA repair and promotes tumorigenesis. *Nature* **563**,
1145 131-136 (2018).
1146 9. Y. Chen *et al.*, A cGAS-mediated mechanism in naked mole-rats potentiates DNA repair and
1147 delays aging. *Science (New York, N.Y.)* **390**, eadp5056 (2025).
1148 10. D. Banerjee *et al.*, A non-canonical, interferon-independent signaling activity of cGAMP
1149 triggers DNA damage response signaling. *Nature communications* **12**, 6207 (2021).
1150 11. Y. Da *et al.*, STING agonist cGAMP enhances anti-tumor activity of CAR-NK cells against
1151 pancreatic cancer. *Oncoimmunology* **11**, 2054105 (2022).
1152 12. L. Deng *et al.*, STING-Dependent Cytosolic DNA Sensing Promotes Radiation-Induced Type I

1153 Interferon-Dependent Antitumor Immunity in Immunogenic Tumors. *Immunity* **41**, 843-852
1154 (2014).
1155 13. E. H. Knelson *et al.*, Activation of Tumor-Cell STING Primes NK-Cell Therapy. *Cancer*
1156 *Immunol Res* **10**, 947-961 (2022).
1157 14. F. Pedretti *et al.*, Harnessing STING Signaling and Natural Killer Cells Overcomes PARP
1158 Inhibitor Resistance in Homologous Recombination–Deficient Breast Cancer. *Cancer research*
1159 **85**, 1888-1908 (2025).
1160 15. H. Zheng *et al.*, Epigenetically suppressed tumor cell intrinsic STING promotes tumor immune
1161 escape. *Biomed Pharmacother* **157**, 114033 (2023).
1162 16. T. Xia, H. Konno, J. Ahn, G. N. Barber, Deregulation of STING Signaling in Colorectal
1163 Carcinoma Constrains DNA Damage Responses and Correlates With Tumorigenesis. *Cell*
1164 *Reports* **14**, 282-297 (2016).
1165 17. K. Bartsch *et al.*, Absence of RNase H2 triggers generation of immunogenic micronuclei
1166 removed by autophagy. *Hum Mol Genet* **26**, 3960-3972 (2017).
1167 18. A. D. Sanders *et al.*, Single-cell analysis of structural variations and complex rearrangements
1168 with tri-channel processing. *Nature Biotechnology* **38**, 343-354 (2020).
1169 19. E. Falconer *et al.*, DNA template strand sequencing of single-cells maps genomic
1170 rearrangements at high resolution. *Nat Methods* **9**, 1107-1112 (2012).
1171 20. K. Grimes *et al.*, Cell-type-specific consequences of mosaic structural variants in hematopoietic
1172 stem and progenitor cells. *Nature genetics* **56**, 1134-1146 (2024).
1173 21. A. D. Sanders, E. Falconer, M. Hills, D. C. J. Spierings, P. M. Lansdorp, Single-cell template
1174 strand sequencing by Strand-seq enables the characterization of individual homologs. *Nat*
1175 *Protoc* **12**, 1151-1176 (2017).
1176 22. D. Porubsky *et al.*, breakpointR: an R/Bioconductor package to localize strand state changes in
1177 Strand-seq data. *Bioinformatics (Oxford, England)* **36**, 1260-1261 (2020).
1178 23. M. Trakala *et al.*, Clonal selection of stable aneuploidies in progenitor cells drives high-
1179 prevalence tumorigenesis. *Genes Dev* **35**, 1079-1092 (2021).
1180 24. E. P. Rogakou, D. R. Pilch, A. H. Orr, V. S. Ivanova, W. M. Bonner, DNA double-stranded
1181 breaks induce histone H2AX phosphorylation on serine 139. *The Journal of biological*
1182 *chemistry* **273**, 5858-5868 (1998).
1183 25. S. So, A. J. Davis, D. J. Chen, Autophosphorylation at serine 1981 stabilizes ATM at DNA
1184 damage sites. *J Cell Biol* **187**, 977-990 (2009).
1185 26. S. Burma, B. P. Chen, M. Murphy, A. Kurimasa, D. J. Chen, ATM phosphorylates histone H2AX

in response to DNA double-strand breaks. *The Journal of biological chemistry* **276**, 42462-42467 (2001).

27. A. J. Pierce, R. D. Johnson, L. H. Thompson, M. Jasin, XRCC3 promotes homology-directed repair of DNA damage in mammalian cells. *Genes & Development* **13**, 2633-2638 (1999).

28. S. Brzostek-Racine, C. Gordon, S. Van Scoy, N. C. Reich, The DNA damage response induces IFN. *J Immunol* **187**, 5336-5345 (2011).

29. F. McNab, K. Mayer-Barber, A. Sher, A. Wack, A. O'Garra, Type I interferons in infectious disease. *Nature reviews. Immunology* **15**, 87-103 (2015).

30. S. Shreeram *et al.*, Wip1 Phosphatase Modulates ATM-Dependent Signaling Pathways. *Molecular Cell* **23**, 757-764 (2006).

31. Z. You, C. Chahwan, J. Bailis, T. Hunter, P. Russell, ATM activation and its recruitment to damaged DNA require binding to the C terminus of Nbs1. *Molecular and cellular biology* **25**, 5363-5379 (2005).

32. R. S. Williams *et al.*, Nbs1 flexibly tethers Ctp1 and Mre11-Rad50 to coordinate DNA double-strand break processing and repair. *Cell* **139**, 87-99 (2009).

33. H. Tauchi *et al.*, The forkhead-associated domain of NBS1 is essential for nuclear foci formation after irradiation but not essential for hRAD50[middle dot]hMRE11[middle dot]NBS1 complex DNA repair activity. *The Journal of biological chemistry* **276**, 12-15 (2001).

34. V. A. Smits *et al.*, p21 inhibits Thr161 phosphorylation of Cdc2 to enforce the G2 DNA damage checkpoint. *The Journal of biological chemistry* **275**, 30638-30643 (2000).

35. F. Bunz *et al.*, Requirement for p53 and p21 to sustain G2 arrest after DNA damage. *Science (New York, N.Y.)* **282**, 1497-1501 (1998).

36. S. M. Harding *et al.*, Mitotic progression following DNA damage enables pattern recognition within micronuclei. *Nature* **548**, 466-470 (2017).

37. C. Zierhut, H. Funabiki, Regulation and Consequences of cGAS Activation by Self-DNA. *Trends in Cell Biology* **30**, 594-605 (2020).

38. J. Wu *et al.*, Cyclic GMP-AMP Is an Endogenous Second Messenger in Innate Immune Signaling by Cytosolic DNA. *Science (New York, N.Y.)* **339**, 826-830 (2013).

39. S. Dvorkin, S. Cambier, H. E. Volkman, D. B. Stetson, New frontiers in the cGAS-STING intracellular DNA-sensing pathway. *Immunity* **57**, 718-730 (2024).

40. Q. Wang, A. M. Bode, T. Zhang, Targeting CDK1 in cancer: mechanisms and implications. *npj Precision Oncology* **7**, 58 (2023).

41. R. Falahat *et al.*, Epigenetic reprogramming of tumor cell–intrinsic STING function sculpts

1219 antigenicity and T cell recognition of melanoma. *Proceedings of the National Academy of*
1220 *Sciences* **118**, e2013598118 (2021).
1221 42. K. Aden *et al.*, ATG16L1 orchestrates interleukin-22 signaling in the intestinal epithelium via
1222 cGAS-STING. *The Journal of experimental medicine* **215**, 2868-2886 (2018).
1223 43. W. H. Organization, *WHO classification of tumours: Digestive system tumours*. (World Health
1224 Organization (WHO, Lyon, ed. 5th, 2019).
1225 44. H. Felchle *et al.*, Novel Tumor Organoid-Based Mouse Model to Study Image Guided Radiation
1226 Therapy of Rectal Cancer After Noninvasive and Precise Endoscopic Implantation.
1227 *International journal of radiation oncology, biology, physics* **118**, 1094-1104 (2024).
1228 45. S. Atatri *et al.*, Protocol for sub-mucosal orthotopic injection of organoids into murine colon to
1229 study tumor growth and metastasis. *STAR Protoc* **6**, 103887 (2025).
1230 46. M. Iizuka, S. Konno, Wound healing of intestinal epithelial cells. *World J Gastroenterol* **17**,
1231 2161-2171 (2011).
1232 47. C. Trapnell *et al.*, Differential gene and transcript expression analysis of RNA-seq experiments
1233 with TopHat and Cufflinks. *Nat Protoc* **7**, 562-578 (2012).
1234 48. S. Anders, P. T. Pyl, W. Huber, HTSeq--a Python framework to work with high-throughput
1235 sequencing data. *Bioinformatics (Oxford, England)* **31**, 166-169 (2015).
1236 49. M. I. Love, W. Huber, S. Anders, Moderated estimation of fold change and dispersion for RNA-
1237 seq data with DESeq2. *Genome Biol* **15**, 550 (2014).
1238 50. K. Breuer *et al.*, InnateDB: systems biology of innate immunity and beyond--recent updates and
1239 continuing curation. *Nucleic acids research* **41**, D1228-1233 (2013).